Supplementary Information

Metal-organic frameworks for the capture of dissolved CO_2 and generated carbonate ions from water

Jacopo Andreo[a,], Subhajit Dutta[a], Nagore Barroso[a,], Aleksander Ejsmont[b], Bettina Baumgartner[c], Agata Jankowska[b], Jonas Tittel[d], Rafael Marcé[e], Marcin Frankowski[b], Bert M. Weckhuysen[c], Evelyn Ploetz[d,*], Joanna Goscianska[b,*], and Stefan Wuttke[a,f,*]

[a.] *BCMaterials, Basque Center for Materials, Applications and Nanostructures, UPV/EHU Science Park, Leioa, Spain*

[b.] *Faculty of Chemistry, Adam Mickiewicz University, Uniwersytetu Poznańskiego 8, 61-614 Poznań, Poland*

[c.] *Inorganic Chemistry & Catalysis Debye Institute for Nanomaterials Science and Institute for Sustainable and Circular Chemistry, Utrecht University, Utrecht, The Netherlands*

[d.] *Department of Chemistry and Center for NanoScience, Ludwig-Maximilians-Universität München, Munich, Germany*

[e.] *Catalan Institute for Water Research (ICRA), Girona, Spain; University of Girona, Girona, Spain*

[f.] *IKERBASQUE, Basque Foundation for Science, Bilbao, Spain*

[*]Correspondence: evelyn.ploetz@cup.uni-muenchen.de, joanna.goscianska@amu.edu.pl, stefan.wuttke@bcmaterials.net

TABLE OF CONTENT

SUPPLEMENTARY NOTE 1. INSTRUMENTATION

1.1. Scanning electron microscopy (SEM)

To determine the particle size and morphology, we carried out scanning electron microscopy using a Hitachi S-4800 FEG SEM operating at an accelerating voltage of 10 kV (150s, 20mA, zoom at x10.000). Samples were coated with a 10 nm gold layer before SEM experiments in an Emitech K550x ion sputter.

1.2. Powder X-ray diffraction (XRD)

The MOFs' structure was identified by powder X-ray diffraction using the D8 Advance Diffractometer (Bruker) with the copper $K_{\alpha 1}$ radiation (λ = 1.5406 Å). The XRD profiles of MOFs were obtained in the 2θ range of 6–80°, using a 0.05° step size per 1 s at RT. The analysis was conducted for as-synthesized MOFs and materials recovered after CO_2 adsorption from aqueous solutions.

1.3. Thermogravimetric analysis (TGA)

The thermal stability of MOFs, before and after CO_2 adsorption from aqueous solutions, was analyzed using a Setsys 1200 apparatus (Setaram). 10 mg of MOF materials were heated over the temperature range of 30–900 °C at a constant rate of 10 °C/min under 100 cm^3/min flow of nitrogen.

1.4. Low-temperature nitrogen sorption isotherms

Nitrogen sorption experiments were conducted on a Quantachrome Autosorb-iQ MP gas sorption analyzer under continuous adsorption conditions. Prior to measurements, powder samples (100-250 mg) were heated at 180 °C for 2 h and outgassed to 10^{-3} Torr. N_2 isotherms were generated by incremental exposure to nitrogen up to 1 atm in a liquid nitrogen (-196 °C) bath. The Brunauer–Emmet–Teller (BET) analysis was used to determine the specific surface areas of MOF samples. Three consistency criteria were used to determine the range for the fitting of the surface area to the BET equation[1]: *i)* the values of $V(1-p/p_0)$ should increase in the selected pressure range (p/p_0), *ii)* the points used to calculate the BET surface area should yield a positive y-intercept, and *iii)* the pressure range (p/p_0) values corresponding to V_m should be within the BET fitting range.

1.5. Inductively coupled plasma optical emission spectrometry (ICP-OES)

The inductively coupled plasma optical emission spectrometry (ICP-OES; ICPE-9820 with mini-torch; Shimadzu, Japan) was applied for qualitative and quantitative detection of elements (Na, K, Rb, Cs, Mg, Ca, Th, In, S, P, B, Al) in the collected water samples. The apparatus with a radial view (Ca and Mg) and axial view (all elements) was equipped with a CCD detector. To determine the concentration of anions, i.e., SO_4^{2-}, PO_4^{2-}, BO_3^{3-}, calculations were performed from the result of the S, P, and B concentrations. Before the analysis, water samples were filtered through a cellulose membrane (Millipore, 0.45 μm pore size) and acidified with 70% HNO_3 (Sigma Aldrich Merck group, Poznan, Poland). All standard solutions used for the calibration curves were prepared by volume dilution of Na,

K, Rb, Cs, Mg, Ca, Th, In, S, P, B, and Al standard solutions (1000 mg/dm^3). Recorded data were evaluated using OriginPro 2020.

1.6. Measurement of pH

All pH measurements were performed with the use of (1) an Aqualytic Portable meter AL10pH (Germany) in Poznan, (2) a pH 1100 L (VWR, the Netherlands) at Utrecht, or (3) a Seven Easy pH meter (Mettler Toledo; Ohio, USA) at Munich, which were calibrated by buffer solution of pH 4.01, pH 7.00 and pH 9.21.

1.7. Measurement of alkalinity and electrical conductivity

The brine salinity, *i.e.*, the electrical conductivity, was measured in-field immediately after collection using a WTW Multi 3630 IDS sensor. The total alkalinity was measured by potentiometric titration with a Methrom, 848 Titrion plus system using the Gran method to calculate it from acidic volumes. The titration acid was 0.05 M HCl. Duplicate measurements were made for each sample, and the precision error was ±1 μmol/kg.

1.8. Total inorganic carbon (TIC) analysis

Carbon dioxide dissolves and reacts in water to carbonic acid, followed by dissociation to bicarbonate and hydrogen carbonate. We determined the Total Carbon (TC), Total Organic Carbon (TOC), and Total Inorganic Carbon (TIC) concentration in the liquid phase using catalytic high-temperature combustion by means of a TOC-L analyzer (Shimadzu; Japan) equipped with an additional nondispersive infrared (NDIR) sensor for CO_2 detection. This method relies on the catalytic oxidation of samples by combustion at 680 °C inside the tubes filled with a platinum catalyst. We carried out experiments on solutions before/after the adsorption of inorganic carbon species to MOFs. TC and TOC values were measured directly via the TOC-L analyzer. TIC values were derived from the difference between the two others.

1.9. *Steady-State* Fourier-transform infrared spectroscopy (FTIR) in transmission

The infrared spectra of MOF materials were registered using an FTIR Bruker IFS 66v/S 161 spectrometer in transmission mode in a wavenumber range of 400-4000 cm^{-1}. The potassium bromide pellets served as the matrix of the testing substance. MOF powders of ~ 1 mg were grounded with anhydrous KBr (~200 mg), followed by tablet formation. Recorded data were evaluated using Opus 5.6 software and then processed via OriginPro 2020.

1.10. Correlative two-photon microscopy with *in situ* Raman spectroscopy

Raman mapping and confocal two-photon fluorescence images of MOF particles were recorded on a recently published setup dedicated to multi-modal optical spectroscopy and image correlation analysis[2]

(MOSAIC). Briefly, the setup is based on a confocal scanning microscope (TE 300; Nikon) with brightfield illumination and camera. We used a fiber-based, frequency-doubled erbium laser (FemtoFiber dichro bioMP; Toptical Photonics) running at 774 nm as the excitation source for two-photon imaging. The excitation laser line for Raman spectroscopy was as DPSS CW laser at 532 nm (Cobolt Samba, 04-01, 100 mW; Sweden). The laser powers amounted to 9.7 mW at 774 nm and 10.6 mW at 532 nm and were determined at the backport of the microscope body. The laser light was coupled into the microscopy via a dichroic mirror (zt532NIRrpc; AHF Analysetechnik) that separates the excitation from the detection path. The excitation light was focused onto the specimens using a water immersion objective with 1.2 NA (CFI Plan Apo VC 60x water; Nikon) while positioning or scanning of the sample was done using an XYZ piezo stage (BIO3.200; PiezoConcept). The sample response, i.e., the two-photon induced emission during imaging or inelastically scattered light during Raman spectroscopy, was collected by the same objective and guided and detected on two different detection paths.

For two-photon imaging, the emission was recorded on an APD detector (Count Blue; Laser Components) after filtering the emission using a dichroic mirror (BS 647 SP; AHF Analysetechnik), a bandpass filter (580/75; AHF Analysetechnik), a 750-nm short-pass (FES0750; Thorlabs), and a 785 Notch (TECHSPEC OD 6.0 Edmund Optics) to block the 774 nm laser line. The experiments were controlled using a home-written program in C#. The confocal data was afterward extracted and evaluated by PAM[3] and Image J2[4].

For spontaneous Raman spectroscopy, a movable silver mirror guided the scattered light to a spectrograph (Kymera 328i; Oxford instruments) equipped with an emCCD camera (iXon 897; Andor). Two filters before the spectrometer served to block shorter wavelengths, including Rayleigh scattering at 532 nm (RET 537 LP; AHF Analysetechnik / 532 nm Notch filter, OD6; Edmund Optics). The spectral resolution amounted to 7.2 cm^{-1} (Grating with 600 l/mm and blaze at 500 nm). Raman spectra were recorded using *Andor Solis for Imaging V4.30* (Oxford Instruments) between 280-4500 cm^{-1}. The acquisition time per pixel was set to 25 sec with 6 repeats (UiO-66) and 5 sec with 6 repeats (JUK-8) with an excitation density of 46.3 $mW/\mu m^2$ at the sample plane.

Data analysis was carried out using MATLAB 2020b (MathWorks, Inc.; Natick, MA, USA) and employed to correct for cosmic rays, Rayleigh scattering, and spurious background. For background correction, we recorded a 'Raman' spectrum of the empty coverslide next to the MOF crystal and subtracted its contribution from the measured Raman spectrum of the MOF sample. If necessary, we additionally removed a linear background by spline subtraction.

1.11. *Transient* attenuated total reflectance (ATR)-FTIR spectroscopy

To monitor the sorption process of CO_2 and carbonate species in gas and liquid phase, we used *in situ* Fourier transform-infrared (FTIR) spectroscopy (Perkin Elmer 3 FTIR spectrometer with N_2-cooled MCT detector) in attenuated total reflection (ATR) mode.[5] ATR crystals (20 x 10 x 0.5 mm, 45°) cut

from double side polished Si wafer and a depth of penetration d_p = 0.52 µm (at 1600 cm^{-1}) and an effective pathlength of $d_{e\parallel}$=0.64 µm $d_{e\perp}$=0.32 µm, yielding at total effective pathlength of ($d_{e\parallel}$+$d_{e\perp}$)/2 * N = 9.65 µm with N=20 were used. Si ATR crystals were placed in a home-built aluminum flow cell (Figure S1.1; adapted from Ref. 6) that was placed in the FTIR spectrometer. The temperature of the aluminum flow cell was controlled using a thermoelectric cooling (TEC) controller (TEC-1091, Meerstetter, Switzerland) and a 20 x 20 mm Peltier element (RS components, the Netherlands). For each spectrum, 32 scans were averaged (10 s/spectrum).[6] MOF films were obtained by drop casting MOF suspensions (2 mg MOF powder in 100 µL methanol) onto the ATR crystal and subsequent heating to 80 °C for 30 min.

1.11.1. Adsorption from aqueous phase monitored by ATR-FTIR spectroscopy

Carbonate solutions were applied with 1.5 ml min^{-1} flow using a peristaltic pump (Ismatec, Germany) and 1/16'' PFA tubing.

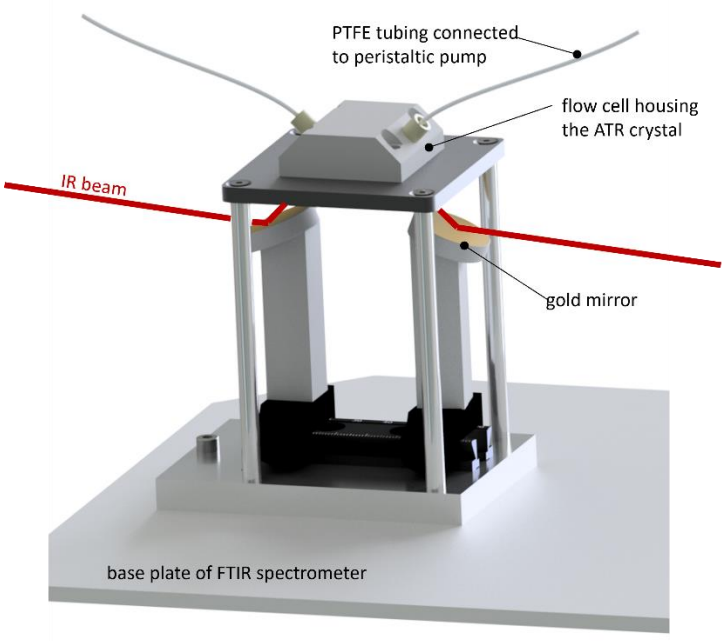

Figure S1.1. FTIR-ATR spectroscopy setup.

1.11.2. Adsorption from gas monitored by ATR-FTIR spectroscopy

CO_2 mixtures were obtained by mixing pure CO_2 (Linde, N.4) and N_2 (Linde, 5.0) streams. Water vapor with different $p/p_0(H_2O)$ was generated by mixing a dry N_2 flow with a moistened N_2 flow obtained from bubbling through water at room temperature by means of mass flow controllers (Bronkhorst) to achieve a total flow of 100 ml min^{-1}. The actual water vapor concentrations were determined by transmission IR spectroscopy in a 10 cm transmission cell with ZnSe windows. For calibration, transmission spectra were integrated in the O-H bending region between 1700-1800 cm^{-1}. Concentrations were obtained from the band areas using reference spectra of 1 ppm/m water from the PNNL database. The application sequence was started with flushing pure N_2 flushing for 10 min.

Subsequently, the partial pressure was increased/decreased and kept for 3 min to reach step to reach equilibrium.

1.12. Data evaluation and representation

If not mentioned otherwise, all data were presented using Origin Pro 2022b (OriginLab Corp.; Northhampton, MA, USA), exported as pdf, and assembled into figures using Adobe Illustrator CS2022 (Adobe Inc.; USA). Crystal structures of MOF samples were visualized using Mercury 2022.3.0 and UCSF Chimera version 1.14[7]. FTIR absorbance spectra were derived from single channels spectra and base line corrected in Matlab R2020b (The Mathworks Inc. USA). Mass flow controllers were controlled using LabView (National Instruments, USA).

SUPPLEMENTARY NOTE 2. PROBING CARBON SPECIES IN WATER BY MOFS

Gaseous carbon dioxide is highly soluble in water and coexists in different chemical species that can interact with the porous scaffold of MOF materials.[8] The following section first describes the chemistry of CO_2 in water at different pHs and its impact on biology. Afterwards we discuss which and why different MOFs were selected for capturing carbon species at different pHs.

2.1. Chemistry of CO_2 in water and its impact in ecosystems

Carbon dioxide dissolves in water and reacts with it to produce carbonic acid (H_2CO_3). Further, H_2CO_3 can be partly dissociated to produce H^+, HCO_3^-, and CO_3^{2-}. The corresponding reaction scheme may be written as:

$$CO_2 + H_2O \underset{k_{-1}}{\overset{k_1}{\rightleftharpoons}} H_2CO_3 \underset{k_{-2}}{\overset{k_2}{\rightleftharpoons}} H^+ + HCO_3^- \underset{k_{-3}}{\overset{k_3}{\rightleftharpoons}} 2H^+ + CO_3^{2-} \quad \text{(eq. 2.1)}$$

Depending upon the pH of the medium, the nature of the carbonic species changes (Figure S2.1). At acidic pH (pH= 2) conditions, the dissolved CO_2 remains as neutral CO_2 molecules. However, going towards higher pH range (pH=6.3), it starts transforming into CO_3^{2-} anions and at pH=6.3, it has the factional contribution of both CO_2 and CO_3^{2-} in which CO_3^{2-} is the predominant species. At pH=8.3, it also transforms into HCO_3^- and effective factional contribution of both HCO_3^- and CO_3^{2-} are present. At more basic pH, i.e. pH=10, the dominating species is HCO_3^-. (Figure S2.1). Hence, the form and concentration of CO_2 are influential in regulating the pH of a water medium. It is observed that with increasing dissolved CO_2 in water, the release of H^+ ions from carbonic acid is also increased, which result in lowering the pH of the medium. As CO_2 level increase in the atmosphere, the amount of dissolved CO_2 also increases, which in turn, increases the amount of carbonic acid and decreases the pH. [9]

As the global anthropogenic CO_2 emission continuously increases (as high as 37.5 billion metric tons till 2022), about 30% of the emitted CO_2 is being dissolved in the ocean and other natural water bodies. As a result, the natural water bodies become more acidic in nature, commonly known as 'ocean acidification' (Figure S2.2).[10] The reduction of pH and increased acidic conditions greatly impact the shell-building aquatic organisms such as mollusks. With increasing ocean acidification scenarios, the free CO_3^{2-} ions bind with H^+, producing lesser CO_3^{2-} ions for calcification for organisms to maintain their shells, skeletons, and other calcium-based structures. In addition, if the aquatic environment becomes too acidic, the shells and skeleton-based components can start to dissolve. Hence, marine organisms could also experience changes in growth, development, abundance, and survival in response to ocean acidification.[9-10]

a)

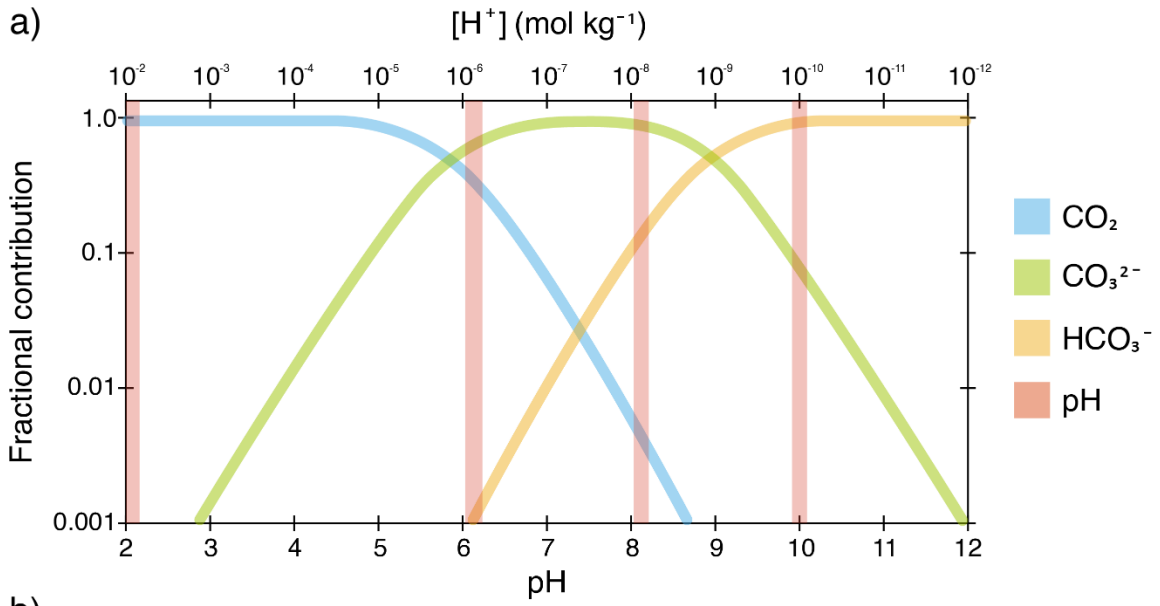

b)

pH	Fractional contribution [CO_2]	Fractional contribution [CO_3^{2-}]	Fractional contribution [HCO_3^-]
2	1	0	0
6.3	0.4	0.6	0
8.3	0.005	1	0.1
10	0	0.1	1

Figure S2.1. (a) Comparison between relative concentration of CO_2 and different carbonate species with different $[H^+]$ concentration and pH values. **(b)** Factional contribution of different carbonate species at different pH.

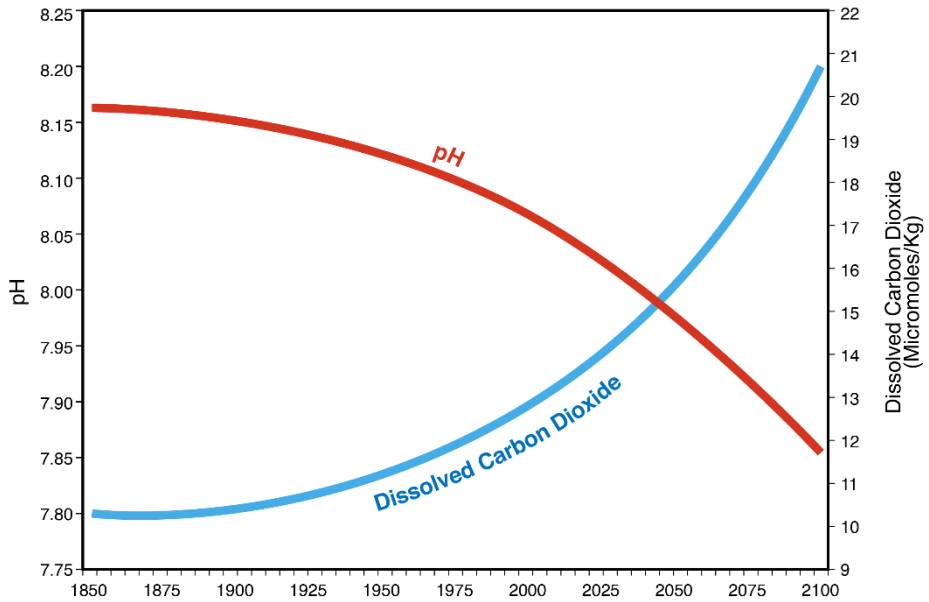

Figure S2.2. Change in ocean pH level and concentration of dissolved CO_2 due to 'ocean acidification' with respect to time.[60]

2.2 Selection process of MOF systems for capturing CO_2

Over the last years, a wide variety of different MOF systems have been developed for CO_2 capture from the gas phase. To select the most auspicious frameworks, we first ran intensive literature research and identified 18 MOF systems that are primarily used for CO_2 capture (Figure S2.2). A detailed overview of their adsorption characteristics is provided in Table S2.1. While the major criteria were a high and selective CO_2 adsorption in the gas phase, we secondly aimed to cover a wide structural diversity in terms of topology and flexibility of the framework as well as a wide range in chemical composition with respect to metal nodes, linkers, and functionalization. Finally, we selected seven MOF systems (Figure S2.3) that either feature a high adsorption capacity or high CO_2 selectivity. We chose ZU-301, which favors CO_2 compared to water and other guest molecules. All other six MOF materials were chosen according to their large uptake capacity. A summary of their physicochemical properties is provided in Figure S2.3.

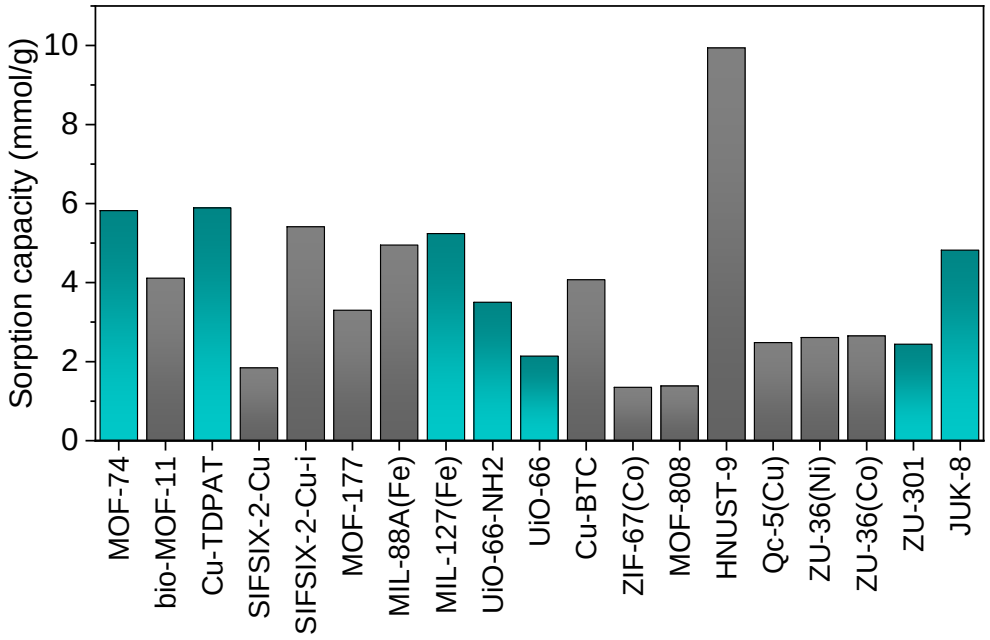

Figure S2.2. Adsorption capacity of MOFs found in the literature. The adsorption capacity values are given in mmol/g of CO_2(g) and are summarized in Table S2.1. All MOFs systems used in this work are highlighted in color.

Table S2.1. Overview of MOF adsorption characteristics dedicated for CO_2 capture in the gas phase.

MOF	Pore size (nm)	BET surface area (m^2/g (N_2))	CO_2 uptake	Adsorption heat (Q_{st}, kJ/mol)	Selectivity (CO_2/N_2)	Ref.
MOF-74 (Mg)	-	1495	35.20 wt% (1atm, 23 °C)	47.0	-	11
MOF-74 (Co)	-	1080	30.60 wt % (1atm, 23 °C)	37.0	-	
MOF-74 (Ni)	-	1070	25.60 wt % (1atm, 23 °C)	41.0	-	
MOF-74 (Zn)	-	816	24.40 wt % (1atm, 23 °C)	-	-	
Bio-MOF-11(Co)	-	1040	4.10 mmol/g (1atm, 25 ºC)	45.0	75.0	12
Cu-TDPAT	0.49	1938	132.00 cm^3 / g (1atm, 25 ºC)	42.2	79.0	13
SIFSIX-2-Cu	1.31	3140	1.84 mmol/g (1bar, 25 ºC)	31.9	13.7	14
SIFSIX-2-Cu-i	0.52	735	5.41 mmol/g (1bar, 25 ºC)	45.0	140.0	
MOF-177(Zn)		2784	3.30 mmol/g (1bar, 25 ºC)		-	15
MIL-88A(Fe)	-	-	4.95 mmol/g (30 ºC)	-	-	16
MIL-127(Fe)	0.12	1436	5.24 mmol/g (1atm, 30 ºC)	-	-	
SIFSIX-14-Cu-i	0.34	612	172.70 cm^3/cm^3	37.7	-	17
UiO-66-NH_2(Zr)	-	1118	3.50 mmol/g (1bar, 25 ºC)		66.0	18
UiO-66(Zr)	-	1321	2.14 mmol/g (1bar, 25 ºC)	17.6	22.0	19
Cu-BTC	0.61 -0.82	1202	4.07 mmol/g (1bar, 25 ºC)	27.0	16.8	20
ZIF-67(Co)	0.75	1726	30.20 cm^3/g	-	39.3	21
MOF-808(Zr)	-	1742	1.38 mmol/g (1atm)	34.0	40.0	22
HNUST-9	0.80 -1.50	2429	4.94 mmol/g (1atm, 25 ºC)	31.5	22.2	23
Qc-5(Cu)	0.22	211.3	2.48 mmol/g (1bar, 25 ºC)	36.2	-	24
ZU-36(Ni)	0.335	-	2.61 mmol/g (1 bar, 25 °C)	55.5	4200.0	25
ZU-36(Co)	0.363	-	2.65 mmol/g (1 bar, 25 °C)	39.1	160.0	
ZU-301(Zn)	0.38	289 m^2/g (CO_2, Langmuir)	2.44 mmol/g (1 bar, 25 °C)	38.9	19000.0	26
JUK-8(Zn)	-	-	108.00 cm^3/g (32 bar, 25 ºC)	-	-	27

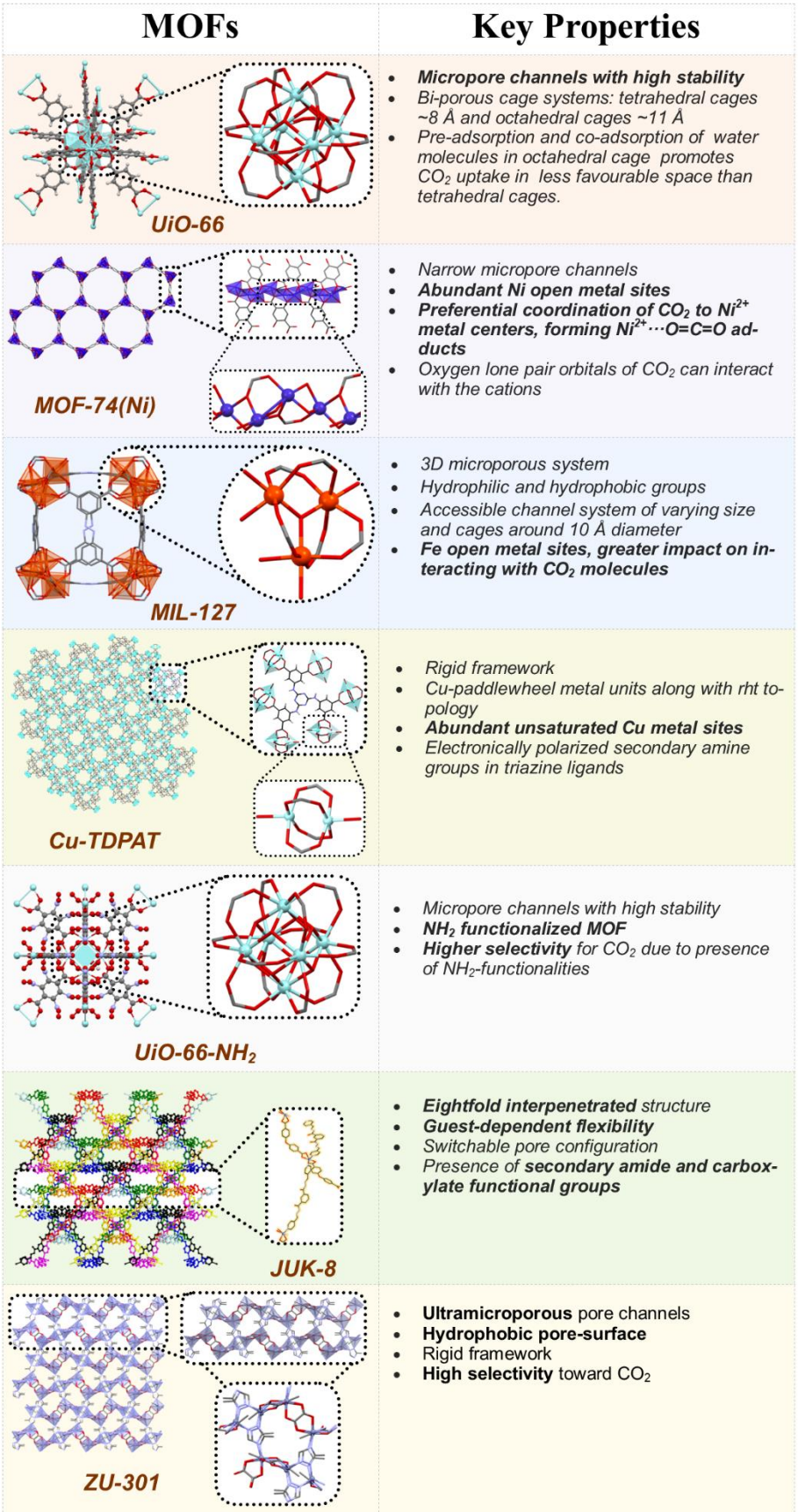

Figure S2.3. Profile of selected MOF materials. The key physiochemical properties related to CO_2 adsorption are summarized on the right per single MOF system. Crystal data information was obtained from: UiO-66,[28] MOF-74(Ni),[29] MIL-127 (Fe),[30] Cu-TDPAT,[31] UiO-66-NH_2,[32] JUK-8,[27] and ZU-301[26].

SUPPLEMENTARY NOTE 3. MOF SYNTHESIS AND CHARACTERIZATION

3.1. Chemicals

Zirconium (IV) chloride ($ZrCl_4$, 98%), iron (III) chloride hexahydrate ($FeCl_3 \cdot 6H_2O$, 99+%), zinc (II) nitrate hexahydrate ($Zn(NO_3)_2 \cdot 6H_2O$, 98%) terephthalic acid (TPA, 99+ %), 2-aminoterephthalic acid (99%), 2-methylimidazole (98%), fumaric acid (99%), cetyltrimethylammonium bromide (CTAB, 99+ %), and oxalic acid (98%) were purchased from Acros Organics. Dimethylformamide (DMF, 99.9% GLR), glucose (99.5%), and formic acid (98%) were purchased from Labkem, zinc(II) carbonate ($Zn(CO_3)_2$, 97 %) from Alfa Aesar, cobalt(II) nitrate ($Co(NO_3)_2 \cdot 6H_2O$, 98%) from Carl Roth, copper(II)nitrate trihydrate ($Cu(NO_3)_2 \cdot 3H_2O$, 99%), 2,5-dihydroxyterephthalic acid (DOBDC, 95%), 3-methyl-1H-1,2,4-triazole (Mtz), 5-nitroisophtalic acid (>99%), 5-aminoisophthalic acid (>98%), cyanuric chloride (>98%) and pyridine-4-carboxaldehyde (97%) were purchased from Fluorochem. Nickel(II) nitrate hexahydrate ($Ni(NO_3)_2 \cdot 6H_2O$, extra pure) was purchased from Fischer Scientific. Isophthalic acid di-hydrazide (99.9%) was purchased from BLDpharm and hydrochloric acid (37%), sodium hydroxide (98%), and sodium bicarbonate (99%) from Labbox.

3.2. Synthesis of linkers

3,3,5,5'-azobenzenetetracarboxylic acid (H_4-TazBz). An already reported procedure was followed with minor modifications[33]. Briefly: to 150 ml of distilled water, 10 g of 5-nitroisophtalic acid were added to a 1 neck 1 L round bottom flask. Under gentle stirring, 25 g of NaOH was added in 5 aliquots of roughly 5 g each, waiting for each aliquot to completely dissolve before adding the next one. The pink mixture was then heated to 60 ºC and 50 g of glucose dissolved in the minimum amount of water (65 ml) was added slowly. Initially, the pink slurry turned into a clear yellow solution and immediately turned into a brown suspension. The heating was stopped 15' after the complete addition of the glucose solution. The mixture was left at room temperature under high stirring (1500 rpm) for 40 hours, capping the round bottom flask with a drip catcher to ensure air recirculation and avoid any product losses. The mixture was then filtered, dissolved in the minimum amount of water, acidified at pH 1 with 6 M HCl, and filtered again. The orange precipitate was dispersed once in water and 3 times in ethanol and filtrated to wash the final impurities. NMR ^{1}H (500 MHz, d_6-DMSO): 13.7 (4H), 8.63 (6H).

2,4,6-tris(3,5-dicarboxylphenylamino)-1,3,5-triazine (H_6TDPAT): An already reported procedure was followed with minor modifications[34]. Briefly: 140 ml of distilled water, 7.6 g of 5-aminoisophthalic acid, 2.7 g of NaOH and 4.35 g of $NaHCO_3$ were combined in a 3-necked 0.5 L round bottom flask equipped with a condenser and a dropping funnel. The mixture was stirred over an ice bath until the internal temperature reached 0 ºC. A solution of 1.82 g of cyanuric chloride in 40 ml of freshly distilled 1,4-dioxane was added to the mixture dropwise over 45-60 minutes, avoiding the reaction temperature to rise over 5 ºC. After complete addition, the ice bath was removed and the mixture was allowed to reach room temperature and then heated to 100 ºC and left to react for 24 hours. The resulting clear

solution was then transferred over an ice-bath and its pH was adjusted to 1 with a 6 M HCl solution. The white precipitate was collected by filtration, rinsed with water several times, and then dissolved in a 2 M solution of NaOH and crushed out again at pH 1 with 6 M HCl. Rinsed with water three times and dried under a high vacuum overnight. NMR ^{1}H (500 MHz, d_6-DMSO): 12.96 (6H), 9.65 (3H), 8.45 (6H), 8.10 (3H).

N'1,N'3-bis[(E)-(pyridin-4-yl)methylidene]benzene-1,3-dicarbohydrazide (pip·EtOH·H_2O). An already reported procedure was followed with minor modifications[35]. Briefly: 350 ml of ethanol, 2.9 g of isophthalic acid dihydrazide and 50 mg of trichloroacetic acid were added to a 3-necked 1 L round bottom flask equipped with a condenser and a dropping funnel and heated to sustained reflux. A solution of 3.1 ml of pyridine-4-carboxaldehyde in 60 ml of ethanol was added over 30-45 minutes. After complete addition, the reaction was left for 1 hour at reflux and let cool overnight. The white precipitate was then filtered and washed repeatedly with ethanol. NMR ^{1}H (500 MHz, d_6-DMSO): 12.28 (2H), 8.67 (4H), 8.47 (3H), 8.15 (2H), 7.69 (5H).

3.3. Synthesis of MOF materials

UiO-66. Zirconium chloride (0.886 g, 3.72 mmol) and terephthalic acid (0.623 g, 3.71 mmol) were dissolved in a mixture of DMF (100 ml) and formic acid (14 ml, 0.37 mol). The mixture was placed in an oven at 120 °C for 24 h. Subsequently, it was allowed to cool down, and the solid was recovered by centrifugation. It was washed by centrifugation (18000 rpm, 30 min, 84 ml) 2 times redispersing each time in DMF. A TCL lamp was used to make sure that there was no more terephthalic acid in the supernatant after the last centrifugation step in DMF. In order to change the solvent, the sample was split into two tubes and centrifuged (18000 rpm, 1 h, 84 ml) three-fold in EtOH.

MOF-74(Ni). In a 500 ml round bottom flask $Ni(NO_3)_2·6H_2O$ (3.80 g, 13.00 mmol) and DOBDC (1.15 g, 1.15 mmol) were suspended in 300 ml of a 1:1:1 DMF, EtOH, and H_2O solvent mixture. The mixture cleared to a green solution at 80 ºC and was kept at 125 ºC for 1 hour. Then, 0.5 ml of concentrated aqueous ammonia was added, and the flask was kept at 125 ºC for 48 hours. The resulting precipitate was filtered, washed twice with DMF for 2 h at 80 ºC, then twice with water for 2 h, and twice with ethanol at room temperature for 1 day. The resulting olive-green powder was dried in the air at room temperature.

MIL-127. In a round bottom flask containing 50 ml of DMF, $FeCl_3·6H_2O$ (34.4 g, 127 mmol) and H_4-TazBz (22.2 g, 62 mmol) were introduced. Then, the mixture was stirred under reflux for 24 h. The resulting brown solid was recovered by filtration, washed four times with 100 ml of DMF (the first two at 80 °C) and twice with 100 ml of acetone, and then dried under vacuum.

Cu-TDPAT. $Cu(NO_3)_2 \cdot 3H_2O$ (2.416 g, 10 mmol) and H_6TDPAT (1.236 g, 2 mmol) were suspended in 100 ml of DMF in a round bottom flask and sonicated for 5 minutes. The mixture was then heated at 100º C for 24 h. The turquoise precipitate was filtered from the greed solution and washed 2 times for 2 h with 50 ml of DMF at 80 ºC and twice again at room temperature. The solid was then dispersed twice in 50 ml of acetone for 2 and 24 h, respectively, before the final filtration and vacuum drying.

UiO-66-NH_2. Zirconium chloride (0.886 g, 3.72 mmol) and 2-aminoterephthalic acid (0.681 g, 3.71 mmol) were dissolved in a mixture of DMF (100 ml) and formic acid (14 ml, 0.37 mol). The mixture was placed in an oven at 120 °C for 24 h. Subsequently, it was allowed to cool down, and the solid was recovered by centrifugation. It was washed by centrifugation (18000 rpm, 30 min, 84 ml) x 3 dispersing each time in DMF. In order to change the solvent, the sample was centrifuged (18000 rpm, 1 h, 84 ml) three times in EtOH.

JUK-8. $Zn(NO_3)_2 \cdot 6H_2O$ (297 mg, 1.00 mmol), pip·EtOH·H_2O (372 mg, 0.850 mmol) and 4,4'-oxybis(benzenedicarboxylic) acid (H_2oba) (258 mg, 1.00 mmol) were suspended in DMF (16 ml) and H_2O (1.8 ml) by sonication (5 min) and heated in a closed vial at 90 ºC for 4 days. Yellow crystals of JUK-8 open pore (op) were filtered off, washed with DMF, and dried under vacuum at 60 ºC for 30 min.

ZU-301. Oxalic acid (0.603 g, 6.56 mmol), Mtz (2.4 g, 28.9 mol), and zinc (II) carbonate (0.6 g, 1.07 mmol) were added to a 100 ml stainless steel Teflon-lined autoclave, where methanol (54 ml) and water (9 ml) were previously added. The mixture was stirred at room temperature for 30 minutes. The autoclave was sealed and placed in an oven at 180 °C for 48 h. Subsequently, it was allowed to cool down and the solid was recovered by centrifugation. It was washed by centrifugation (21500 rpm, 30 min, 24 ml) x 3 dispersing each time in H_2O. In order to exchange the solvent, the sample was centrifuged (21500 rpm, 1 h, 24 ml) 3 times in EtOH.

3.4. Characterization of MOF materials

All MOF systems were structurally characterized after the synthesis (see Supplementary Notes S3 and S4 for more details). They were investigated with respect to crystallinity and purity by X-ray diffraction. Scanning electron microscopy was used to determine their particle size and morphology (Section S3.5). N_2 sorption experiments confirmed the porosity in line with the literature (Figure S3.8) and thermogravimetric analysis (TGA; Figure S3.9), and FTIR spectroscopy (Figure S3.10) confirmed the composition of the pristine MOF samples. Next, we investigated the host-guest interactions between MOFs and CO_2, respectively carbonate species in solutions of different pH values by different methods, including PXRD, and total inorganic carbon (TIC) analysis. These efforts are described in detail in Supplementary Notes S4 and S5. Shortly, we used PXRD to monitor the stability of the crystal structure after exposure to carbonate solutions (Supplementary Note S4.1). We determined the total amount of inorganic carbon species before and after the adsorption processes in order to determine their maximum uptake capacity (Supplementary Note S5). Next, we employed transient *in situ* vibrational spectroscopy combined with advanced microscopy (Supplementary Note S6) to follow the sorption process in time. We used *in situ* ATR-FTIR spectroscopy in the liquid and gas phase and characterized the sorption process and interacting carbonate species at given pH values for the two most promising materials JUK-8 and UiO-66-NH_2. In combination with correlative *in situ* Raman spectroscopy, we confirmed that water penetrates UiO-66-NH_2 and JUK-8. Supplementary Note S7 provides background information about water samples collected in rivers, reservoirs, weirs, and the Mediterranean Sea along the East Coast of Spain.

3.5. Scanning electron microscopy

3.5.1 UiO-66

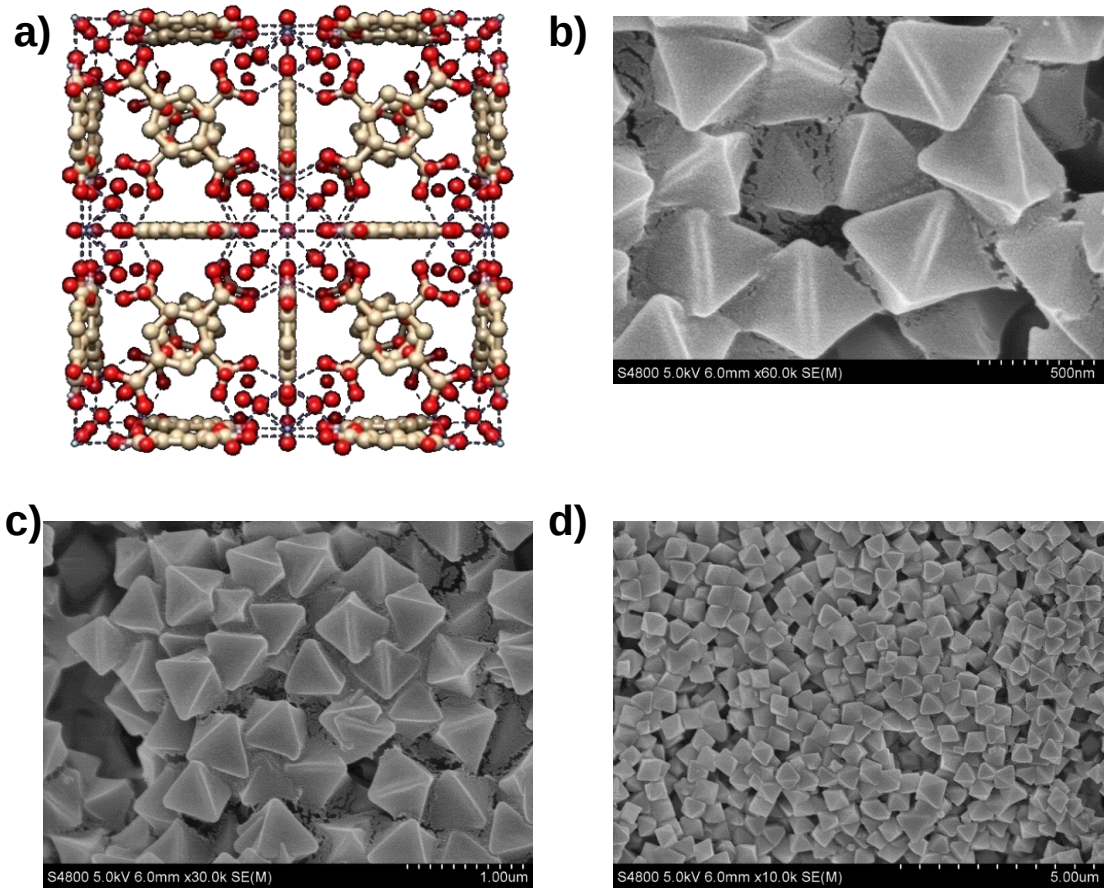

Figure S3.1. UiO-66. (a) Crystal structure, **(b-d)** SEM images at **(b)** 500 nm, **(c)** 1 µm, and **(d)** 5 µm resolution reveal a bipyramidal particle shape with a particle size of around 500 nm.

3.5.2 MOF-74(Ni)

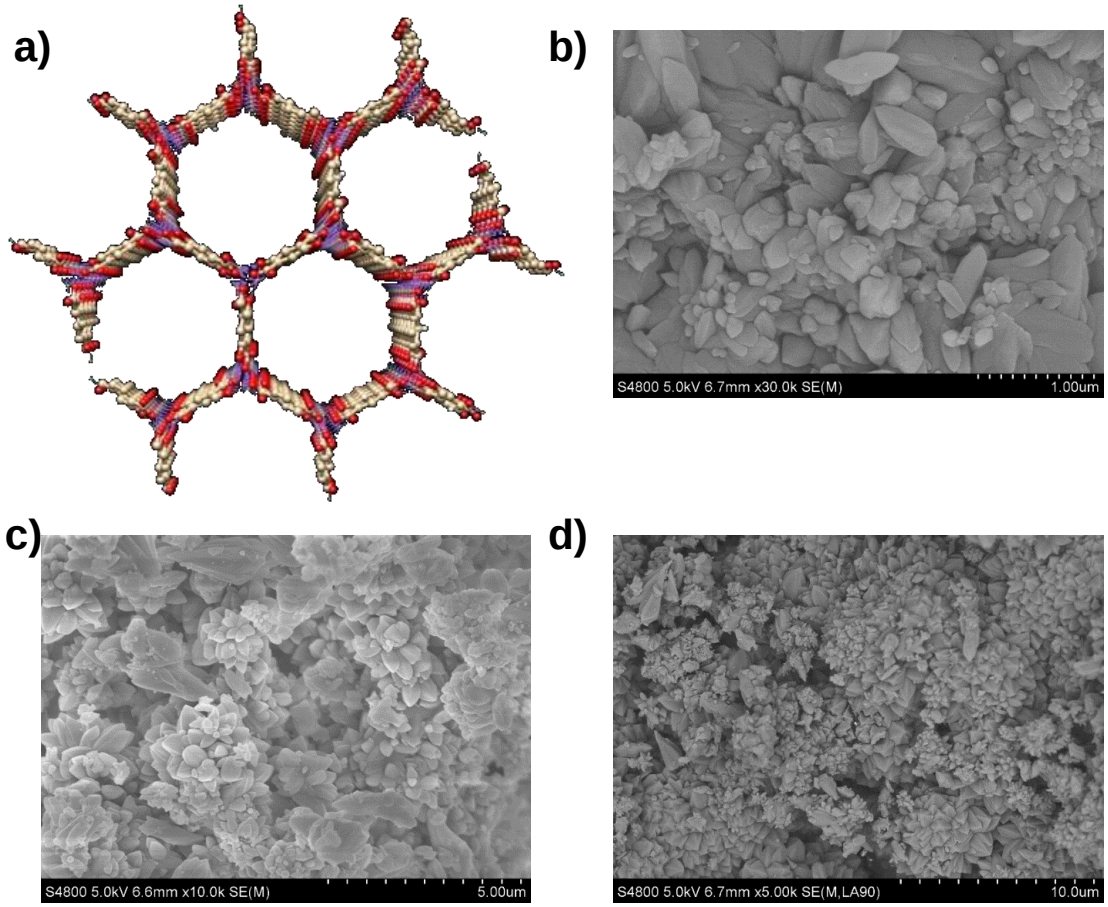

Figure S3.2. MOF-74(Ni). (a) Crystal structure, **(b-d)** SEM images at **(b)** 1 µm, **(c)** 5 µm, and **(d)** 10 µm resolution reveal a cubic particle shape with a particle size of around 2 µm.

3.5.3 MIL-127

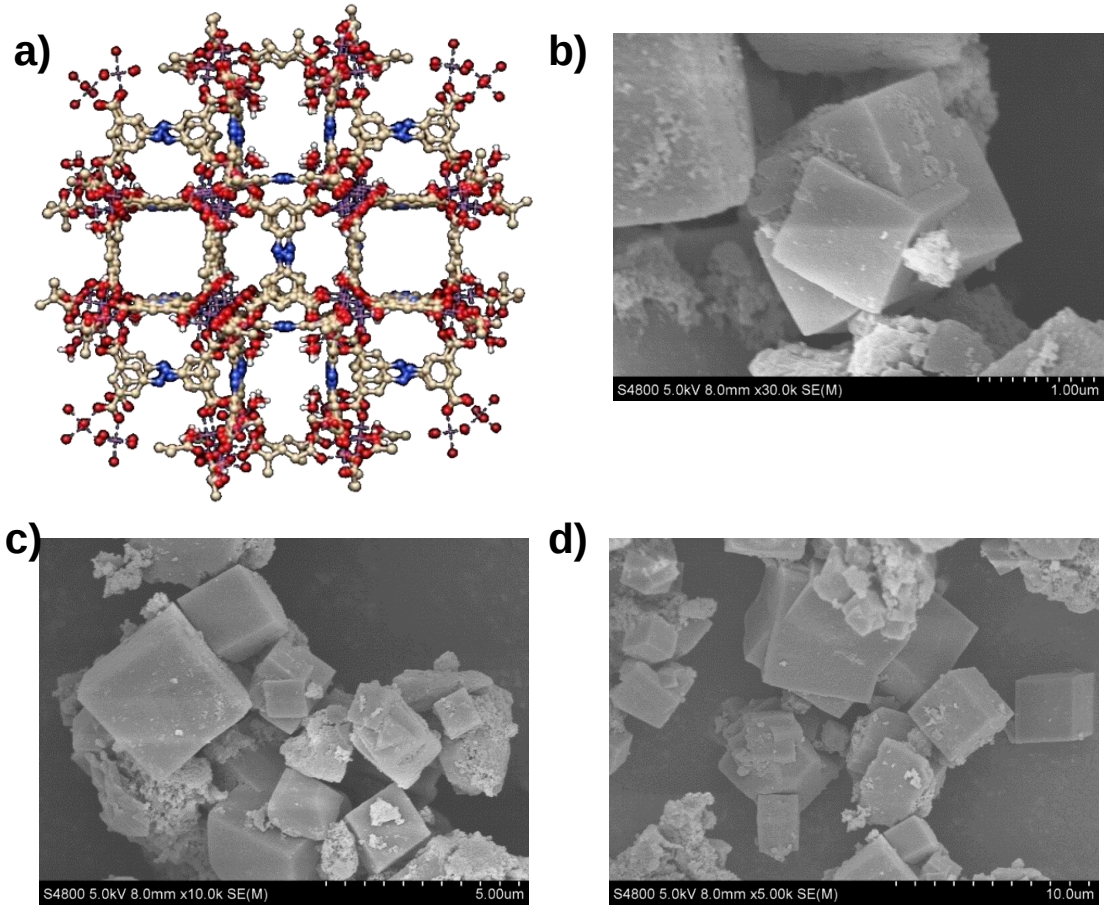

Figure S3.3. MIL-127. (a) Crystal structure, **(b-d)** SEM images at **(b)** 1 µm, **(c)** 5 µm, and **(d)** 10 µm resolution reveal a highly heterogeneous particle shape with sizes in the 1-2 µm range.

3.5.4 Cu-TDPAT

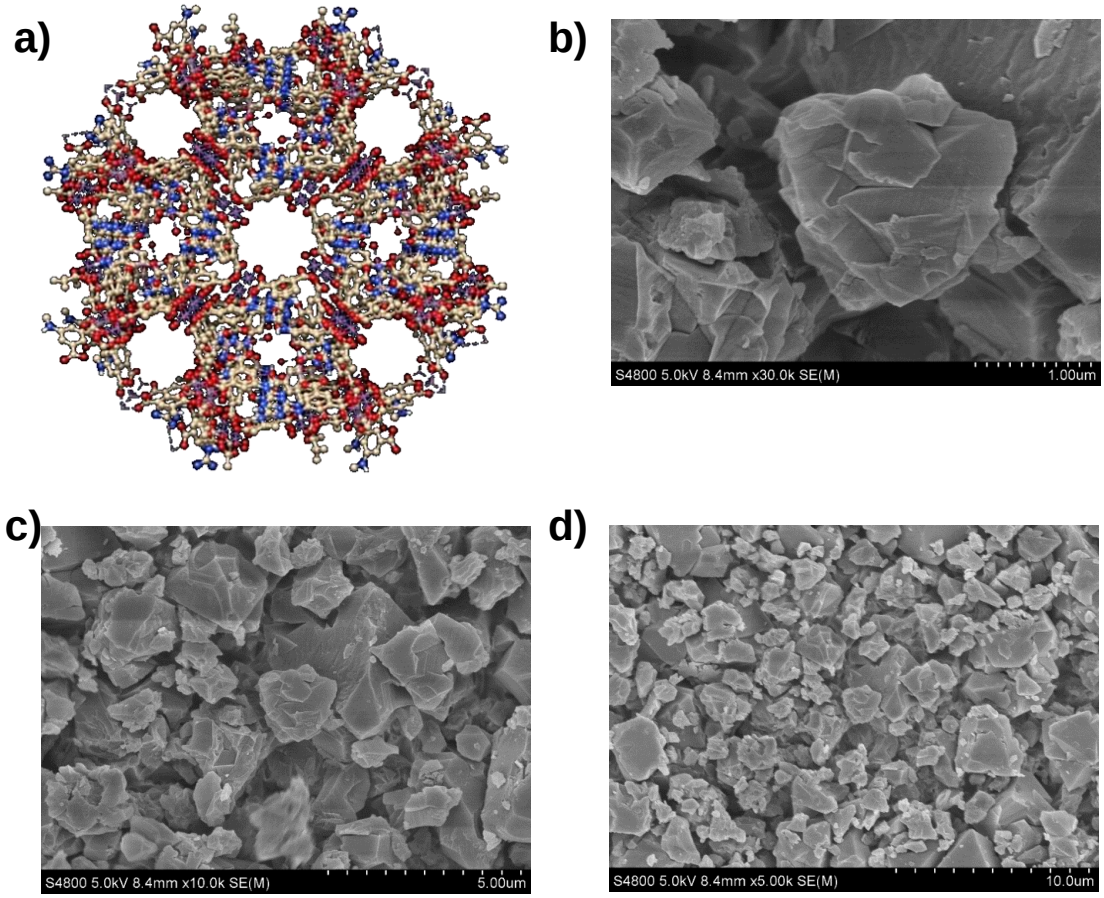

Figure S3.4. Cu-TDPAT. (a) Crystal structure, **(b-d)** SEM images at **(b)** 1 µm, **(c)** 5 µm, and **(d)** 10 µm resolution reveal a highly heterogeneous particle shape with sizes in the ~200 nm range.

3.5.5 UiO-66-NH_2

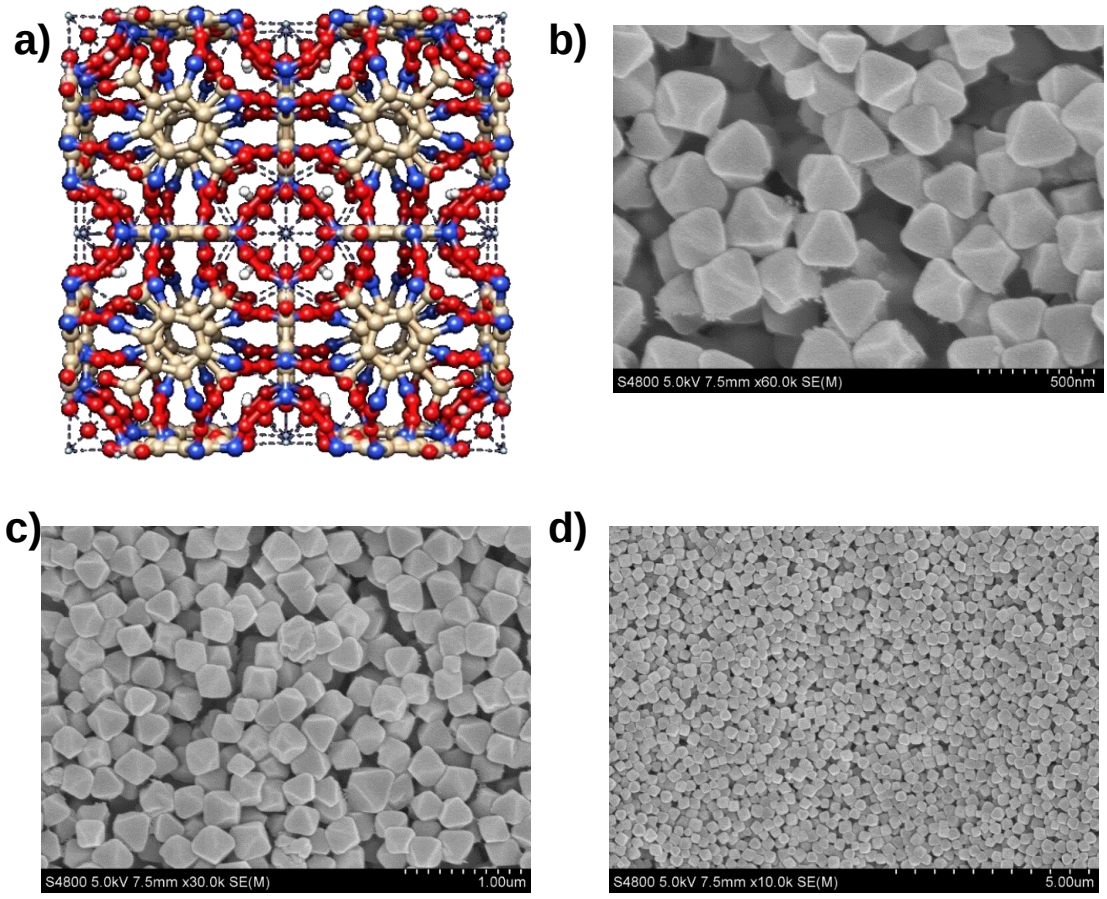

Figure S3.5. UiO-66-NH_2. (a) Crystal structure, **(b-d)** SEM images at **(b)** 500 nm, **(c)** 1 µm, and **(d)** 5 µm resolution reveal a bipyramidal particle shape with sizes around 150 nm.

3.5.6 JUK-8

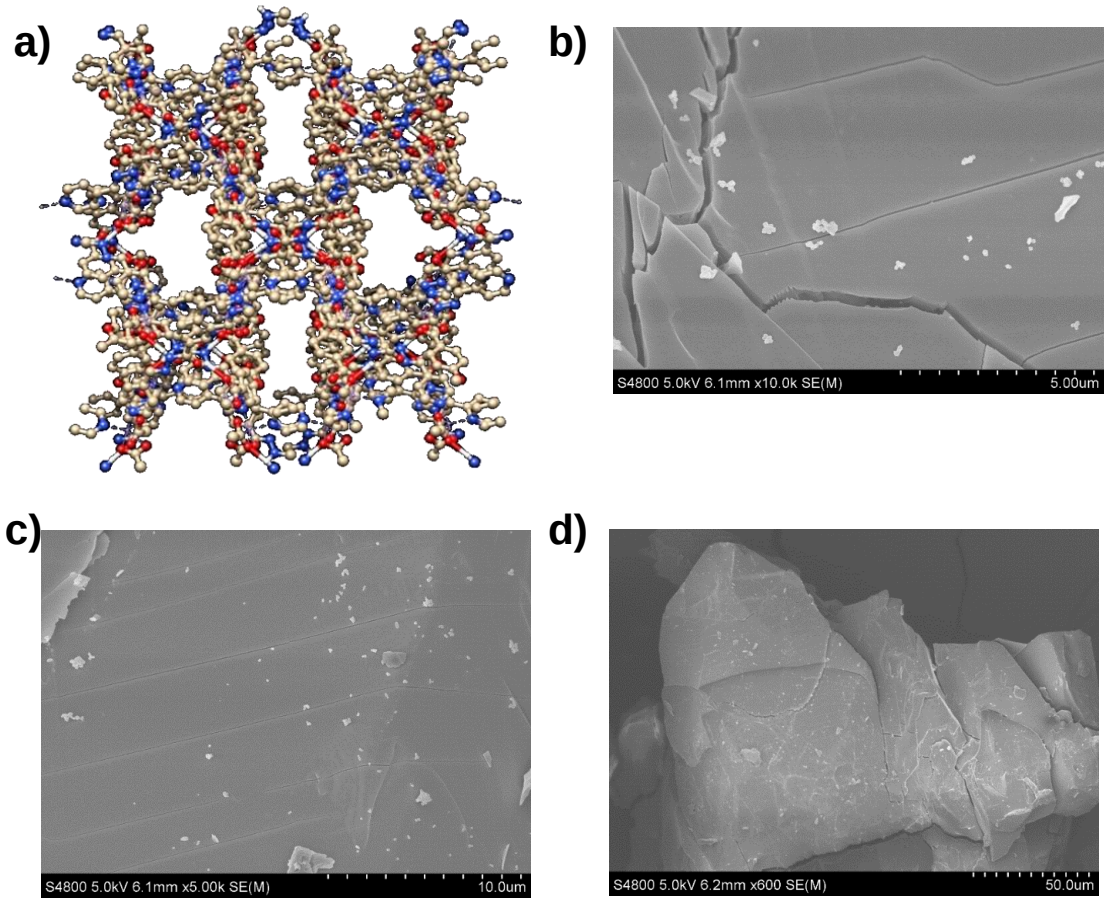

Figure S3.6. JUK-8. (a) Crystal structure, **(b-d)** SEM images at **(b)** 5 µm, **(c)** 10 µm, and **(d)** 50 µm resolution reveal particles with sizes in the range of 0.1-0.2 mm.

3.5.7 ZU-301

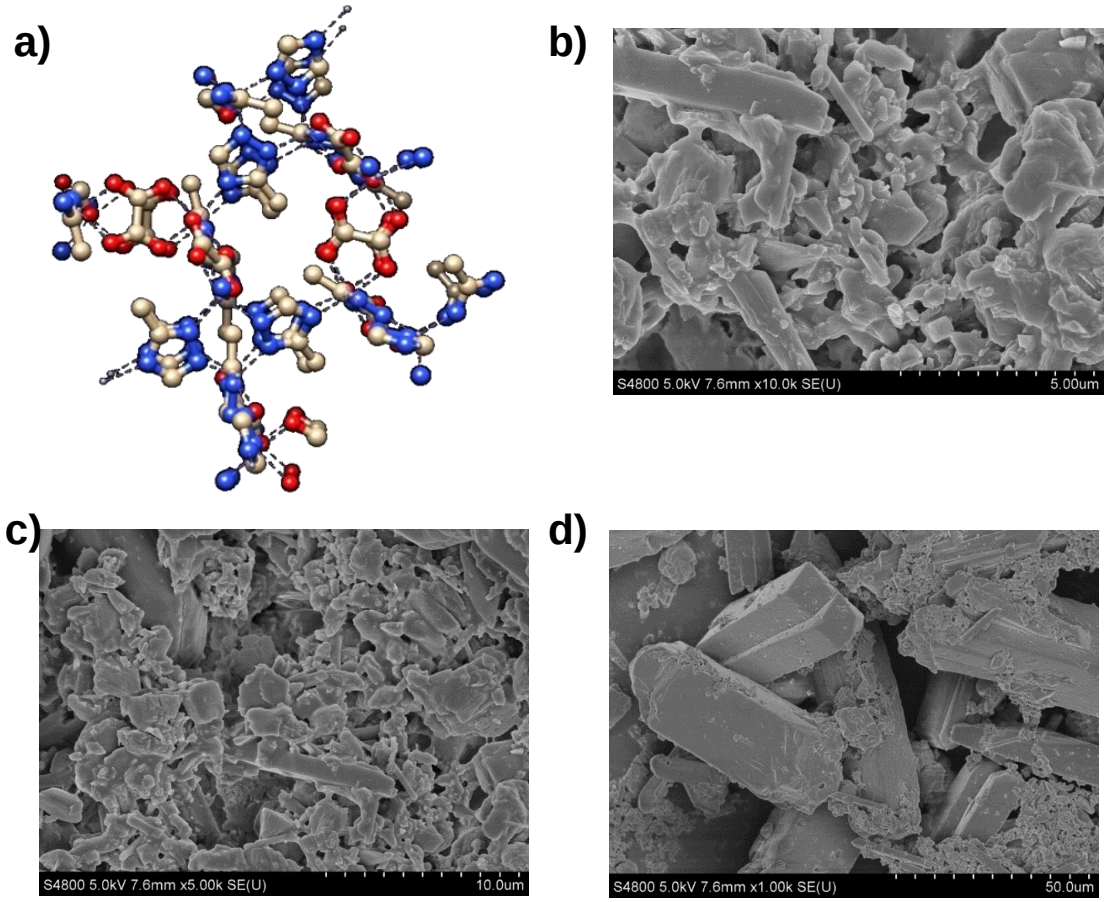

Figure S3.7. ZU-301. (a) Crystal structure, **(b-d)** SEM images at **(b)** 5 µm, **(c)** 10 µm, and **(d)** 50 µm resolution reveal particles with sizes within the 10-50 µm range.

3.6. N_2 adsorption/desorption isotherms

a)

	Surface area (m^2/g)	Pore Volume (cm^3/g)
UiO-66	1299.0	0.61
MOF-74(Ni)	1234.0	0.49
MIL-127	1028.0	0.87
Cu-TDPAT	2161.0	0.49
UiO-66-NH_2	825.0	0.73
JUK-8	1.7	N.A.
ZU-301	7.0	N.A.

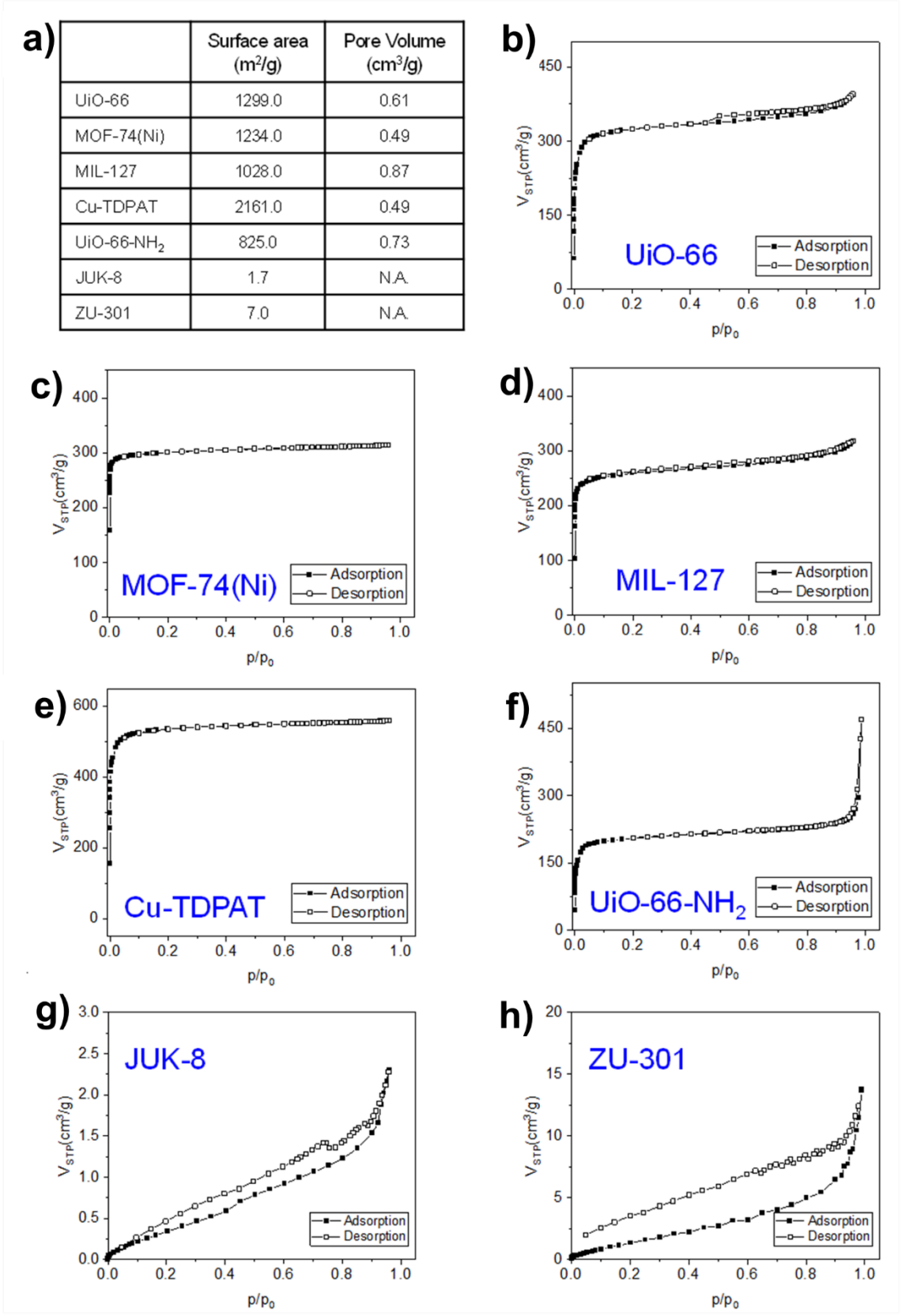

Figure S3.8. N_2 sorption isotherms measured at 77 K. (a) Summary of determined surface areas and pore volumes for all 7 MOF systems. **(b-h)** Adsorption (files dots) and Desorption (open dots) isotherms of **(b)** UiO-66, **(c)** MOF-74(Ni), **(d)** MIL-127, **(e)** Cu-TDPAT, **(f)** UiO-66-NH_2, **(g)** JUK-8, and **(h)** ZU-301.

3.7. TGA analysis

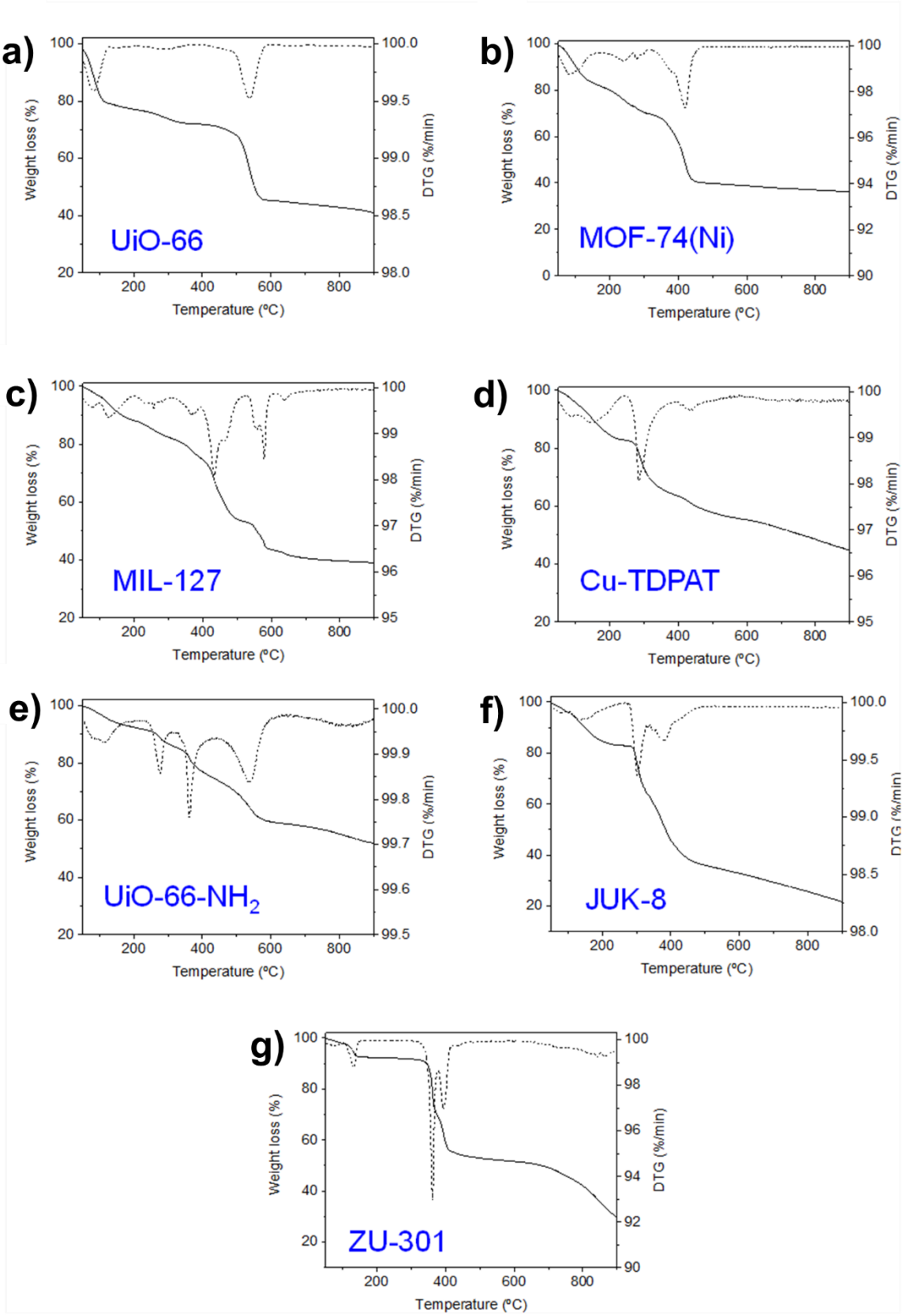

Figure S3.9. Thermogravimetric analyses of pristine MOF samples. TGA curves of **(a)** UiO-66, **(b)** MOF-74(Ni), **(c)** MIL-127, **(d)** Cu-TDPAT, **(e)** UiO-66-NH_2, **(f)** JUK-8, and **(g)** ZU-301.

3.8. FTIR analysis

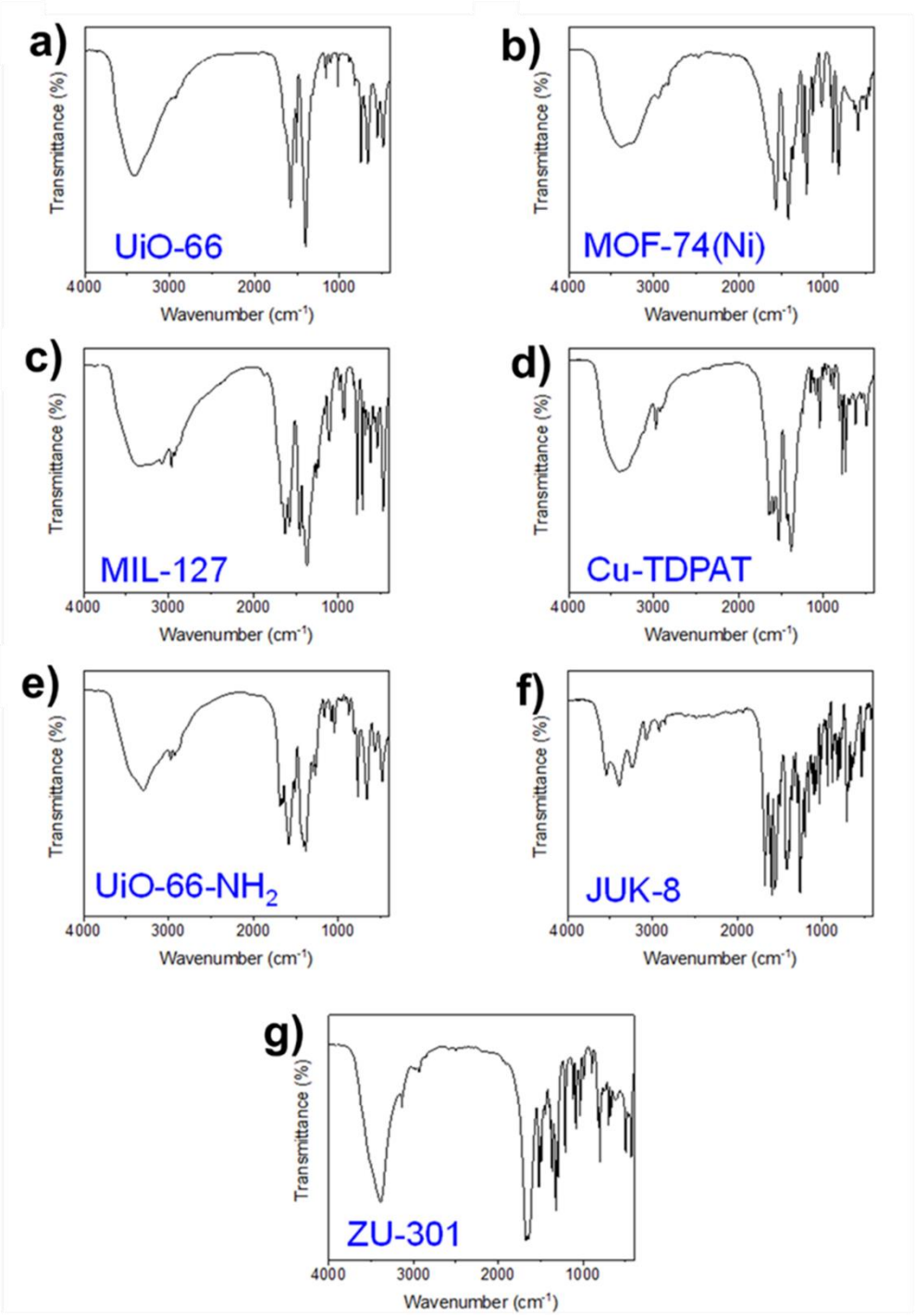

Figure S3.10. FTIR spectra of MOF samples prepared at RT and ca. 30% relative humidity. (a) UiO-66, **(b)** MOF-74(Ni) **(c)** MIL-127, **(d)** Cu-TDPAT, **(e)** UiO-66-NH_2, **(f)** JUK-8, and **(g)** ZU-301. The strong resonance centered around 3300 cm^{-1} and side shoulder around 1650 cm^{-1} is due to adsorbed water molecules from air during the preparation process.

SUPPLEMENTARY NOTE 4. MOFS STABILITY STEADY-STATE ASSAYS

MOF stability is strongly influenced by the pH and ionic strength of solutions the material is in contact with. Although we selected MOFs, which are stable in water, we checked the material stability in the different solutions used for inorganic carbon species adsorption by measuring PXRD directly after adsorption for the most concentrated carbonate solution at all pH values. The diffractograms are shown in Figure S4.1, and the results are summarized in Table S4.1. We found that all MOF systems were stable for pH 10 and pH 8.3. Cu-TDPAT, JUK-8, and ZU-301 were disassembled at pH 2, and Cu-TDPAT and ZU-301 proved to be unstable also at pH 6.3. Minor changes in the diffractograms were observed for MOF-74(Ni) at pH 2 and for MIL-127 over the full pH range, showing that their unit cells are affected by the guest molecules while their frameworks remain crystalline.

Table S4.1. Stability of MOFs probed by PXRD. Green: stable and red: not stable.

MOFs	pH 2	pH 6.3	pH 8.3	pH 10
MIL-127	✓	✓	✓	✓
Cu-TDPAT	✗	✗	✓	✓
MOF-74(Ni)	✓	✓	✓	✓
JUK-8	✗	✓	✓	✓
UiO-66-NH_2	✓	✓	✓	✓
UiO-66	✓	✓	✓	✓
ZU-301	✗	✗	✓	✓

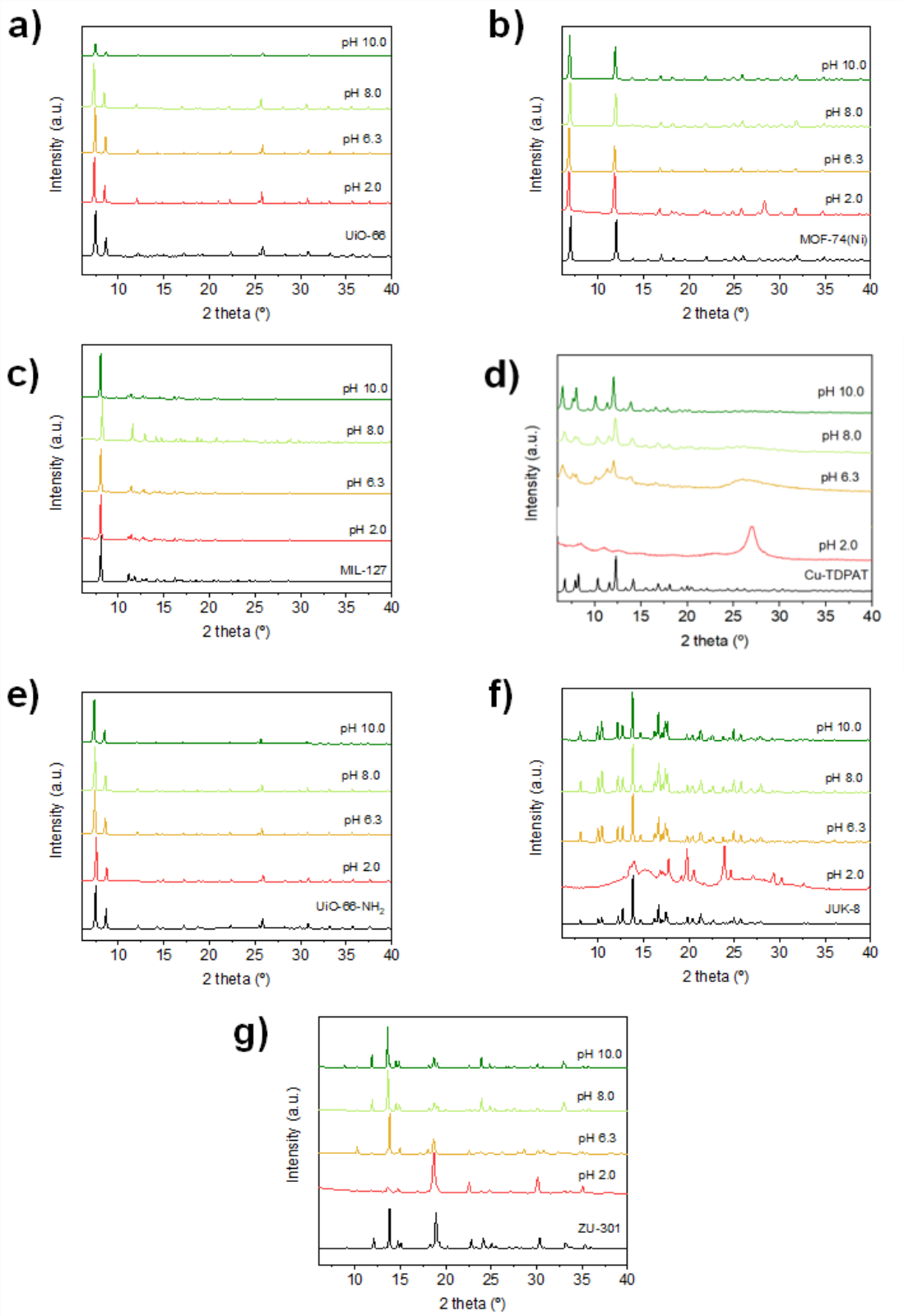

Figure S4.1. PXRD measurements of MOF samples before and after inorganic carbon species adsorption at pH 2, 6.3, 8.3 and 10. (a) UiO-66, **(b)** MOF-74(Ni) **(c)** MIL-127, **(d)** Cu-TDPAT, **(e)** UiO-66-NH_2, **(f)** JUK-8, and **(g)** ZU-301 for the pristine MOF (at the bottom) and pH 2, pH 6.3, pH 8.3 and pH 10 (sorted from bottom to top).

SUPPLEMENTARY NOTE 5. CARBONATE ADSORPTION BY MOFS DEPENDS ON THE PH VALUE. While for many gases like N_2, the amount of dissolved gas in the aqueous phase can be determined from its gas phase concentration via Henry's law[36], it fails for CO_2. At neutral or basic pH, CO_2 reacts with water to form carbonic acid and consecutively bicarbonate and carbonate ions with different ratios, depending on the solution pH and ionic composition[37]. According to its reaction pathway, we selected four different pH values with known concentrations of dissolved carbon species. We expect the following: (1) gaseous CO_2 at pH 2.0, (2) a 1:1 ratio between CO_2 and HCO_3^- at pH 6.3, (3) predominantly hydrogen carbonate HCO_3^- at pH 8.3, and (4) a mixture between HCO_3^- /CO_3^{2-} at pH 10.0.

Controlling the pH and, hence, the ratio of the different inorganic carbon species is an uncertain process, as multiple variables influence the complex equilibrium between the different species. It becomes even more cumbersome when measuring the adsorption capacity of MOF for dissolved carbon species at a given pH, as the adsorption to the framework will further influence the equilibrium among them. We addressed this challenge by not determining the adsorbed amount of carbon species to MOF samples directly but by monitoring the total inorganic carbon concentration (TIC) dissolved in the solution via high-temperature combustion[36,38,39] (Supplementary Note 1.9) before and after the exposure to MOF samples. Since the TIC value includes all forms of inorganic carbon, it is not affected by the equilibrium between the four species independent of the affinity to all four species. Therefore, a decrease in TIC value within the solvent reflects increased adsorption of carbon species onto the MOF material independent of the chemical equilibrium between the different forms.

To investigate the adsorption process, we exposed MOF samples to solutions with a known TIC content, obtained by dissolving varying amounts of $NaHCO_3$ and then using them directly or correcting the pH to 2.0, 6.3, 8.3 and 10. The pH of the solutions was corrected in a closed system by adding HCl (5 mol/l for pH 2.0 and 0.1 mol/l for pH 6.3) or NaOH (0.1 mol/l for pH 10.0) solutions. Concentrations of $NaHCO_3$ solutions before adjusting to a proper pH varied and were in the range of 40–640 mg/l (for pH 2.0), 5–150 mg/l (for pH 6.3 and 8.3), and 10–150 mg/l (for pH 10.0).

To measure MOF adsorption, 41.5 ml of solution was added to 25 mg of each MOF. Afterward, samples were placed in an IKA KS 4000i control incubator shaker for 4 h. In the next step, MOF materials were separated by centrifugation and the residual total inorganic carbon (TIC) and total organic carbon (TOC) concentrations in the solutions were determined. The TIC/TOC measurements, before and after the adsorption processes, were performed using an HTC system, namely a TOC-L analyzer (Shimadzu) equipped with the nondispersive infrared (NDIR) sensor for CO_2 detection.

To establish the amount of the adsorbed inorganic carbon species (Q_e) from aqueous solutions in various conditions, the following formula was applied:

$$Q_e = \frac{(C_0 - C_e) \cdot V}{m} \qquad \text{(eq. 5.1)}$$

where:
C_0 − initial inorganic carbon species concentration (mmol/l),
C_e − the inorganic carbon species concentration (mmol/l) remaining after the adsorption process,
V − the volume of the adsorbate solution (L),
m − the mass of the MOF material (g).

We characterized the uptake of carbonate species from water by plotting the total amount of adsorbed inorganic species Qe as a function of the concentration of inorganic carbon species Ce remaining after the adsorption process. The total amount Qe specified was given as the maximum value of the recorded uptake. At pH 2, differences in TIC values directly report on the uptake of carbon dioxide by the different MOF frameworks. We compared the measured CO_2 uptake in the liquid phase to the uptake behavior reported in the literature in the gas phase and found an adsorption capacity, which is reduced by more than 50% in presence of water (Figure S5.1). This finding is in contrast to gas phase measurements of CO_2 uptake based on IR spectroscopy in the presence of water vapor (see Supplementary Note S6.5), which shows that the uptake capacity is strongly reduced by the incorporation of water in the framework.

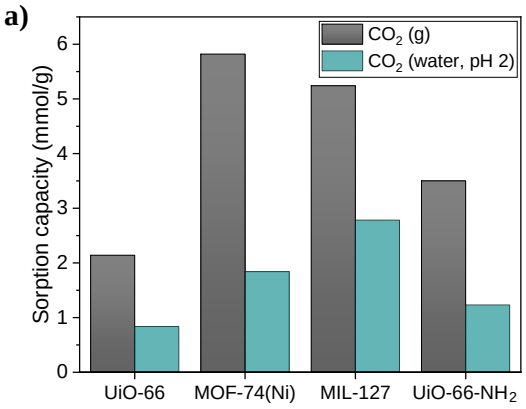

Figure S5.1. Uptake behavior at pH 2. CO_2 adsorption in the gas phase (see Table S2.1 and Figure S2.1) is more than 2-fold more efficient than adsorption to frameworks in the presence of water at pH2.

The adsorption capacity of the materials was evaluated by this methodology as a function for all pH values. A detailed summary of the results recorded at pH 2, 6.3, 8.3, and 10 is given in Figure S5.2.

a)

	maximal q_e (mmol/g)			
	pH 2	pH 6.3	pH 8.0	pH 10
UiO-66	0.84	0.69	0.64	0.47
MOF-74(Ni)	1.84	0.36	0.33	0.53
MIL-127	2.78	1.42	0.55	0.66
Cu-TDPAT	N.A.	N.A.	0.44	0.42
UiO-66-NH_2	1.23	0.90	0.88	1.16
JUK-8	N.A.	6.79	0.63	0.47
ZU-301	N.A.	N.A.	0.17	0.02

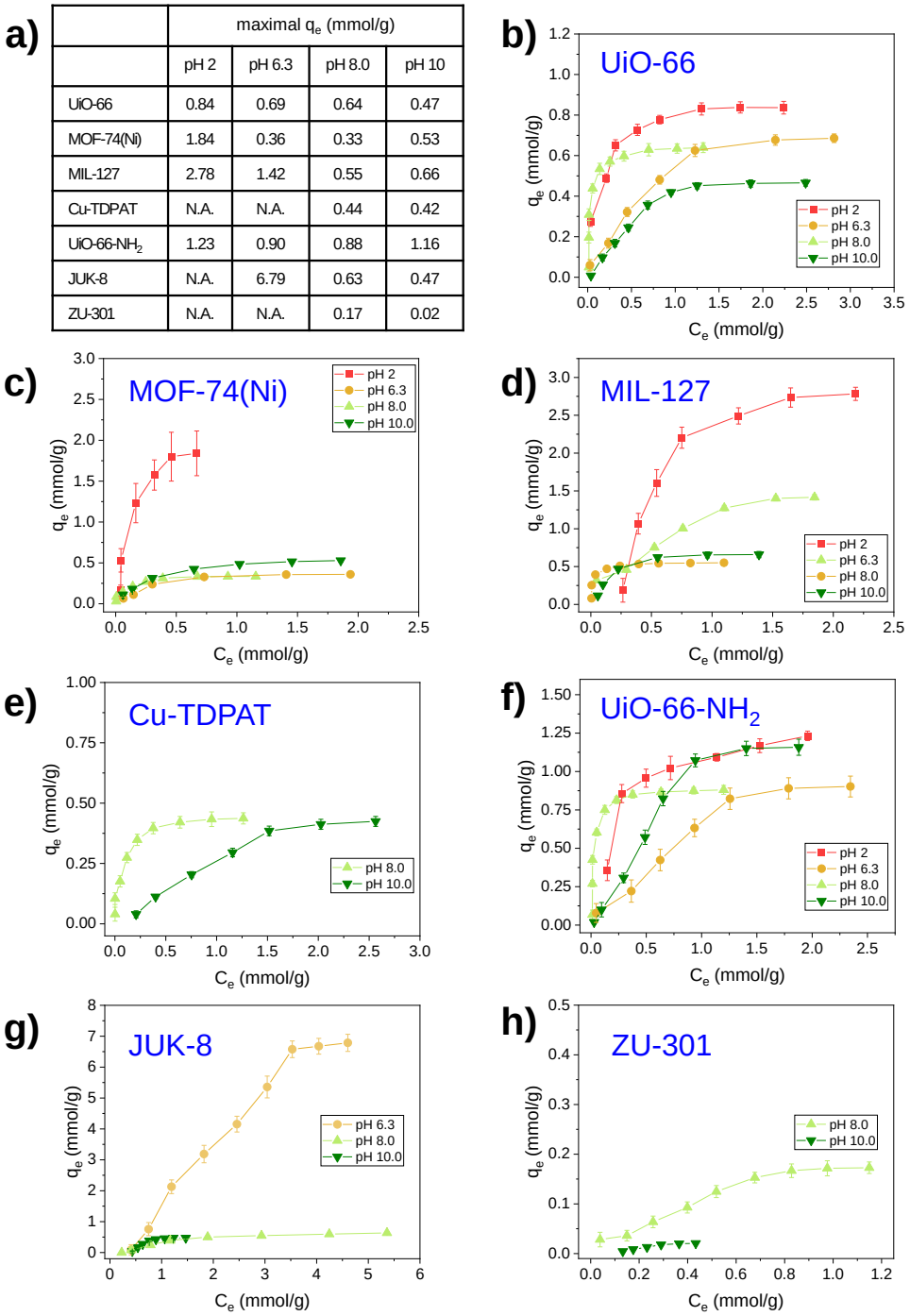

Figure S5.2. Adsorption isotherms of carbon inorganic species from solution by MOFs at different pH values. **(a)** Summary of maximum adsorption capacities (Qe) detected for the 7 MOF samples at different pHs. **(b)** UiO-66, **(c)** MOF-74(Ni), **(d)** MIL-127, **(e)** Cu-TDPAT, **(f)** UiO-66-NH_2, **(g)** JUK-8, and **(h)** ZU-301 determine the amount of adsorbed carbon species Qe after exposure to aqueous carbonate solutions at pH 2, 6.3, 8.3 and 10 for 4 hours.

SUPPLEMENTARY NOTE 6. SPECTROSCOPIC IN-SITU CHARACTERIZATION OF HOST-GUEST INTERACTIONS.

Raman and infrared spectroscopy are two complementary techniques probing the vibrational signature of molecules. They are label-free and usually noninvasive and nondestructive. We made use of both techniques to monitor different aspects of the complex process in which carbonate adsorption into MOFs is taking place. We employed *steady-state* Fourier Transform IR spectroscopy (FTIR) spectroscopy to characterize MOF samples after synthesis and to determine their stability at different pH. ATR-FTIR was chosen for *time-resolved* measurements to further cope with the strong water adsorption in the case of water-containing samples. While IR spectroscopy benefits from its fast data acquisition and the fact that spurious contributions of fluorescence are not detected in the IR, we chose *space-resolved* Raman microspectroscopy for probing host-guest interaction inside micron-sized, single MOF crystals due to the low signal interference of water and the good spatial resolution of ~ 270 nm. Lastly, we used Raman, as well as ATR-FTIR spectroscopy, to decipher and monitor which carbonate species interact with the selected MOF samples UiO-66-NH_2 and JUK-8 in the aqueous and gaseous phases.

In order to discuss the carbonate adsorption of MOFs, i.e., the observed spectroscopic signatures of MOFs and the different carbonate species, via difference spectra in the main text (Figure 5), we started with a bulk characterization. Supplementary Note 6.1 shows images of single MOF particles obtained by two-photon imaging, which were characterized afterwards by Raman and IR spectroscopy for a band assignment of the pristine MOF materials as well as the saturated $NaHCO_3$ solutions and CO_2 (Supplementary Note 6.2). We additionally included data on UiO-66, allowing for a specific band assignment in comparison to UiO-66-NH_2. Next, we showed that the presence of water at different pH values does not interfere with the vibrational signature of the already hydroxylated MOF systems (Supplementary Note 6.3). Supplementary Note 6.4 summarizes and discusses the spectroscopic signatures of carbonate species in solution and during adsorption to UiO-66-NH_2 and JUK-8 as probed in time-series measurements via ATR-FTIR spectroscopy in Figure 5. Next, we benchmarked the amount of adsorbed CO_2 in gaseous and aqueous solutions and showed that the affinity of both MOF frameworks to it is affected and reduced in the presence of water molecules (Supplementary Note 6.5-6.6). Lastly, we employed spontaneous Raman mapping (Supplementary Note 6.7) for visualizing that water species penetrate the JUK-8 framework.

6.1. Particle characterization of UiO-66, UiO-66-NH_2, and JUK-8

As shown in Supplementary Note S3.5, UiO-66, and UiO-66-NH_2 were originally synthesized as bipyramidal particles with 500 nm and 200 nm in diameter, while JUK-8 formed 50 µm sized particles. We used two-photon imaging to investigate the size and morphology of particles, which were afterwards studied by vibrational spectroscopy to investigate the host-guest interaction between carbonate species and the framework.

UiO-66 (Figure S6.1; top) showed strong two-photon-excitation induced auto-fluorescence, which facilitated the visualization of µm-sized particles by scanning TPE microscopy. Particles are made up of clustered nanoparticles (as highlighted by the white boxes and stripe artifacts due to floating nanoparticles in water). Also, UiO-66-NH_2 forms µm-sized clusters of nanoparticles (Figure S6.1; middle), however with lower nonlinear imaging response. As expected from the synthesis and SEM imaging, JUK-8 consists of crystals of several µm in diameter (Figure S6.1; bottom).

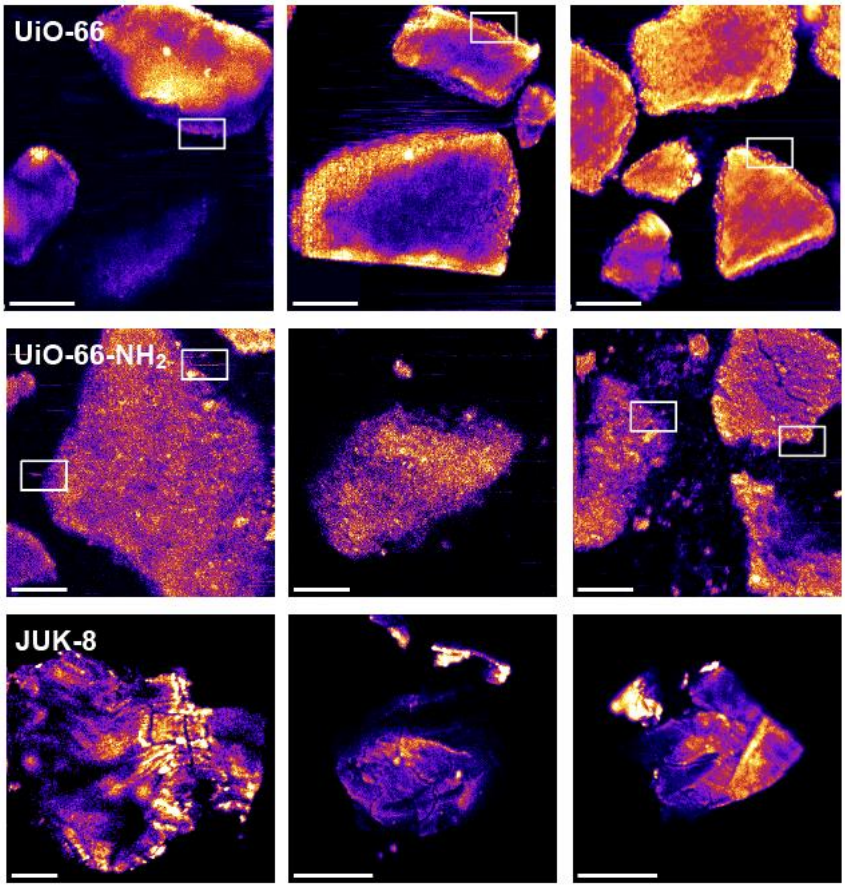

Figure S6.1. Two-photon imaging of MOF particles in water. (top) UiO-66 particles are made up of small nanoparticles. **(middle)** UiO-66-NH_2 nanoparticles cluster into 50 µm sized particles. **(bottom)** JUK-8 has a crystalline structure with particles between 20-40 µm as expected from SEM (Supplementary Note 3.5). Scale bar: 20 µm.

6.2. Characterization of pristine material by ATR-FTIR and Raman spectroscopy

Raman spectra were recorded under constant N_2 flow on hydroxylated MOFs. FTIR spectra were taken from hydroxylated MOFs prepared at RT / air with ca. 30% relative humidity. All recorded FTIR spectra show, therefore, a side shoulder around 1650 cm^{-1} and a strong band centered at 3300 cm^{-1} due to adsorbed water molecules. The latter obscures the FTIR signature of the μ_3:OH stretch vibration of hydroxyl groups bound to the inorganic cluster at ~ 3675 cm^{-1} and the NH-stretch vibrations at ~3520 and ~3400 cm^{-1} originating from linker molecules of the MOFs. Weak bands around 2850-3100 cm^{-1} are due to aliphatic and aromatic CH stretching modes.

6.2.1. UiO-66

The fingerprint region (900-1200 cm^{-1}) of UiO-66 (Figure S6.2) is dominated by two contributions: the carboxylate stretching vibrations around 1450 and 1600 cm^{-1} and different C-C vibrational modes due to relative movements of carboxylate-linker, linker-linker, and the benzene ring. Between 700-1200 cm^{-1}, primarily CH and OH bending modes contribute to the spectrum. Vibrational modes involving the movement of groups as part of the inorganic clusters are observed in the low-frequency range. An extensive description of both spectra and animations of vibrational modes can be found in the literature[40-42]. A short summary is given in Supplementary Table S6.1).

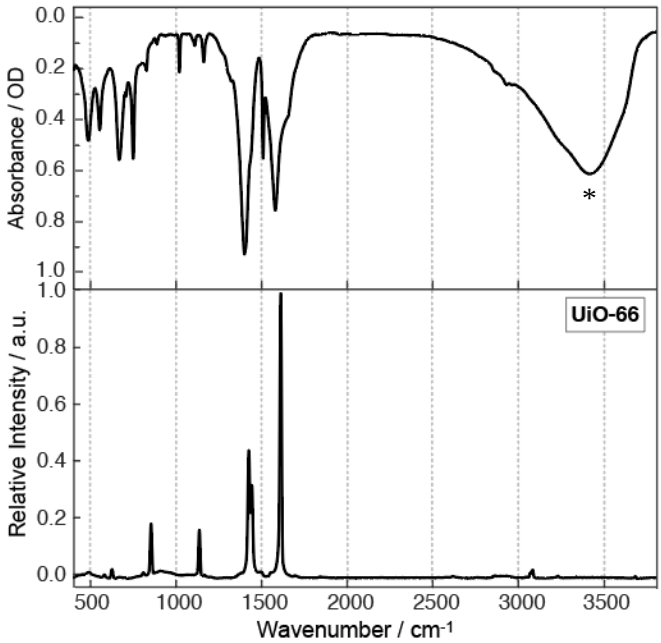

Figure S6.2. FTIR and Raman spectra of UiO-66. (top) The ATR-FTIR spectrum was measured after preparation in ambient air with ca. 30% humidity. **(bottom)** The Raman spectrum of the dry UiO-66 aggregates was recorded at 532 nm excitation with an integration time of 150 seconds under constant N_2 flow.

Table S6.1. Band assignment for UiO-66. Abbreviations: ν: bond stretching; ρ: rocking (in-plane); δ: planar angle bending; β: in-plane bending; γ: out-of-plane bending (wagging); φ: deformation; χ: aromatic ring breathing; i.p: in-plane; o.o.p: out-of-phase; sh: shoulder. (*) Vibrational signatures due to Water.

IR	Lit.	Ref.	Assignment	Raman	Lit.	Ref.	Assignment
484	470	[40-42]	ν_{AS} (Zr-OC)	**498**	**493**	[40,41]	$\nu(\mu_3\text{-O})$
551	556	[40-42]	ν_{AS} (Zr-OC)	590	589	[40,41]	β(CC-C) carboxylate/aromatic bending
665	673/655	[40-42]	$\nu(\mu_3\text{-O})$	**634**	634	[40,41]	γ(COO-)
746	746/743	[40-42]	δ(COO-) + δ(OH) + $\nu(\text{C-C})_{ring}$				
815	814/822	[42]	δ(OH) + δ(CH) o.o.p	815	818	[40,41]	β(OH)
884	885	[42]	ρ(CH)	**866**	862	[40,41]	β(OH) + $\nu(\text{C-C})_{ring}$
1017	1020/1016	[42]	$\gamma(\text{CCC})_{\varphi}$ + δ(OH)				
1094	1083	[42]	DMF				
1159	1160/1157	[40-42]	β(CH) + δ(CH)	**1144**	1145	[40,41]	χ(ring)
1395	1395/1392	[40,41]	ν_S(COO-) / ν(C=C) + δ(C=C−C)	1428	1434	[40,41]	ν(C=C) + δ(C=C−C)
				1448	1454	[40,41]	ν_S(COO-) i.p.
1506	1507/1507	[40-42]	ν_{AS}(COO-) + $\nu(\text{C-C})_{ring}$				
1576	1584/1571	[40,41,43]	ν_{AS}(COO-)				
1662	1662	[42]	DMF: (C=C)	**1615**	1615	[40,41]	$\nu(\text{C-C})_{arom.}$
2849			DMF: aliphatic ν(CH)				
2927			DMF: aliphatic ν(CH)				

6.2.2. UiO-66-NH_2

As reported in the literature[41,44], UiO-66-NH_2 is highly fluorescent, even for laser excitation at 785 nm. The detection of its spectroscopic features is, therefore, quite challenging. We faced strong fluctuations in the background hampering the detection of weak Raman bands and the absolute intensity of vibrational transitions. The observed Raman resonances (Table S6.2), however, are in good agreement with earlier reports[41,43-46].

While the underlying vibrational signature[40-42] of UiO-66 is still preserved in UiO-66-NH_2, the addition of amino groups to the linker leads to further bands in the fingerprint region (Figure S6.3): the NH scissor (bending) movement $\delta(NH_2)$ of the NH_2 groups at 1621 and 1495 cm^{-1}, and the twisting and rocking NH stretch vibration at 1296 and 1163 cm^{-1}, as well as the aromatic CN stretching vibration $\nu(C_{ar}\text{- N})$ at 1257 cm^{-1}. Further, strong bands at 1018 and 1657 cm^{-1} are associated with incorporated DMF during synthesis.

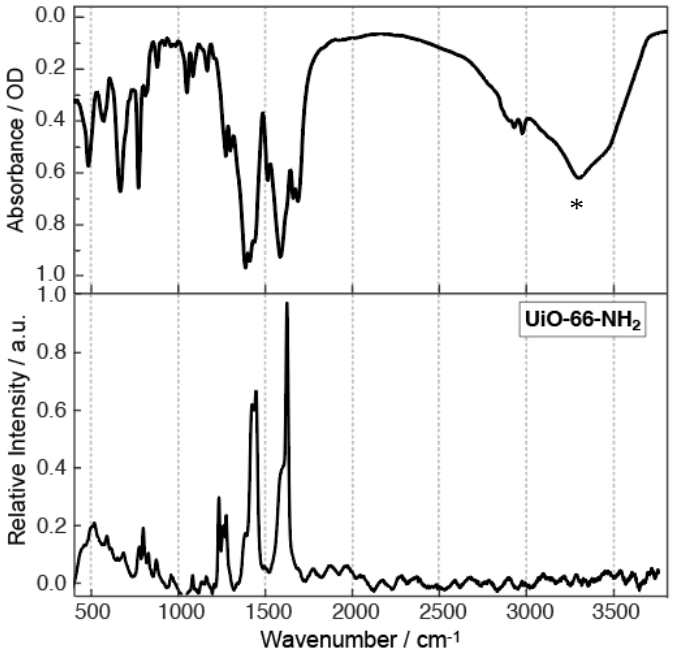

Figure S6.3. FTIR and Raman spectra of UiO-66-NH_2. (top) The ATR-FTIR spectrum was measured for MOFs crystals exposed to 30 % humidity. **(bottom)** The Raman spectrum of the pristine MOF crystal was recorded at 532 nm excitation with an integration time of 150 seconds under constant N_2 flow. Strong fluorescence contributions cause large fluctuations in the background and hamper the detection of weak Raman bands.

Table S6.2. Band assignment for UiO-66-NH_2. Abbreviations: ν: bond stretching; ρ: rocking (in-plane); δ: planar angle bending; β: in-plane bending; γ: out-of-plane bending (wagging); φ: deformation; τ: twisting; χ: aromatic ring breathing; i.p: in-plane; o.o.p: out-of-phase; sh: shoulder. (*) Vibrational signatures due to Water.

IR	Lit	Ref.	Assignment	Raman	MOF	Ref.	Assignment
481			ν_{AS} (Zr-OC)	**520**	**493**	[40,41]	$\nu(\mu_3\text{-O})$
567			$\nu(\mu_3\text{-O})$	**593**	589	[40,41]	β(CC-C) carboxylate/aromatic bending
665	662	[47]	DMF: δ(O=C-N)	**621**	634	[40,41]	γ(COO-)
768	766	[41]	δ(OH) + γ(CH)	**800**	802	[41]	δ(COO-) + δ(C-H)
809	814	[43]	δ(OH) + δ(CH) o.o.p.	**830**	833	[41]	β(COO-)
1018	**1019**	[46]	$\gamma(CCC)_{\varphi}$ + δ(OH)	**873**	866	[40,41]	$\beta(OH) + \nu(C\text{-}C)_{ring}$
1094	1091	[47]	DMF: $\gamma(CH_3)$ N	**1128**	1132	[41]	δ(CH) + ρ(C-N)
1163	**1161**	[41]	ν_S(COO-) / β (CH)	**1162**			ν_S(COO-) / β (CH)
				1234	1235	[41]	β(C-H) + ν(N-H)
1269	1258	[41,48]	β(CH) + τ(C-N)	**1257**	1257	[41]	β(C-H) + ν(C-N)
1296	1276	[41]	ν(C=C) + ν(N-H) + β(C-H)	**1275**	1276	[41]	ν(C=C) + ν(N-H) + β(C-H)
1383	1383	[41]	ν_S(C-COO-) + ν(C=C)	**1385**	1379	[41]	ν_S(C-COO-) + ν(C=C)
1405	1408	[43]	ν(COO-)	**1429**	1418	[41]	ν(C=C) + ν(C-C) + β(C-H)
1495	1499	[41]	ν_{AS}(COO-) + δ(CH)+ν(NH)	**1447**	1450	[41]	ν_S(COO) + ν(C=C) + $\delta(NH_2)$
1511	1550	[46]	ν_{AS}(COO-)+ν(C=C)				
1583	1579/1589	[41,44,45]	ν_{AS}(COO-)	**1590**	1588	[41]	ν(C=C) + $\delta(NH_2)$
1621	1626	[48]	δ(NH)	**1625**	1627	[41]	ν_S(C=C) + $\delta(NH_2)$
1657	1653	[47]	DMF: ν(C=O)				
2850		[47]	DMF: aliphatic ν(CH)				
2918		[47]	DMF: aliphatic ν(CH)				

6.2.3. JUK-8

Lastly, we characterized the vibrational signature of JUK-8 by Raman and FTIR spectroscopy. JUK-8 shows strong breathing behavior with the pore-opening transformation between a closed (cp) and open pore (op) associated with a volume change[49,50]. The pore opening happens upon the adsorption of guest molecules such as CO_2 or H_2O. We, therefore, decided to characterize the host framework in the presence of water molecules in the open form JUK-8op, as this resembles the active form of the material being in an aqueous solution. JUK-8 is a zinc-based framework $[Zn(oba)(pip)]_n$ made up of 8 interpenetrated diamondoid (*dia*) subnetworks[49,50]. Here, the two linker systems pip (4-pyridyl functionalized benzene-1,3-dicarbohydrazide) and oba (4,4′-oxybis(benzenedicarboxylic) acid) complex with Zinc to form one of the 8 intertwined ***dia*** subnetworks (Figure S6.4a).

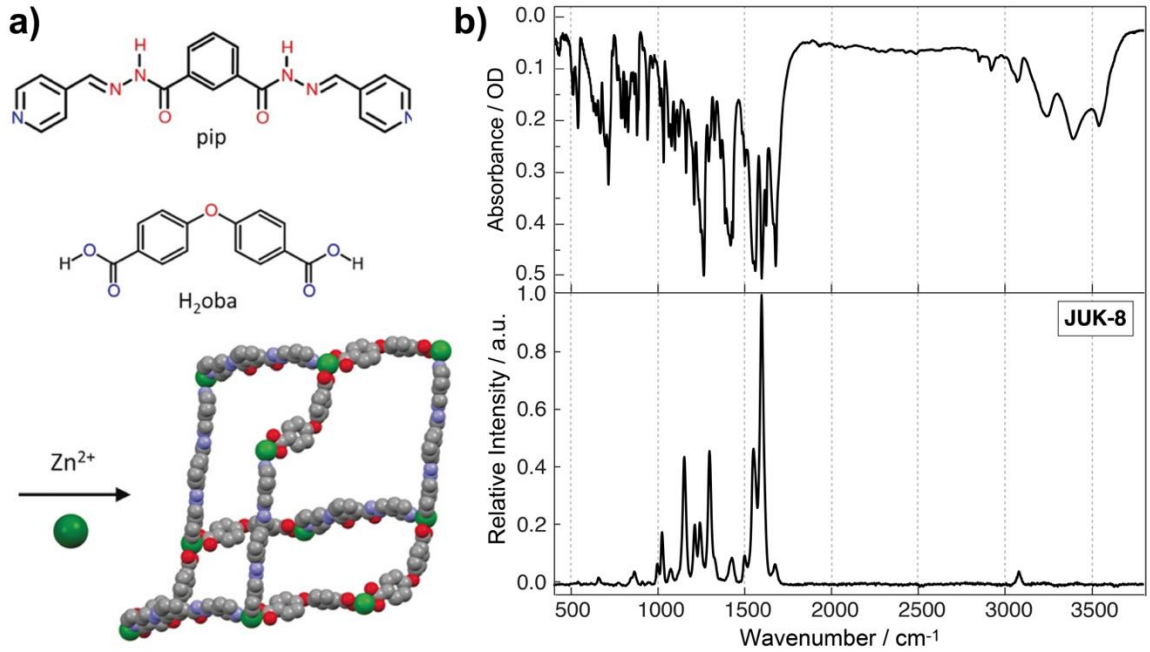

Figure S6.4. FTIR and Raman spectra of JUK-8. (a) Zinc, together with the organic building blocks *pip* and *H_2oba* forms one of the intertwined, eight ***dia*** subnetworks that constitute the JUK-8 framework. Reprinted with permission from Roztocki et al. [49]. Published 2020 by Wiley-VCH. **(b)** Vibrational spectra. **(top)** The ATR-FTIR spectrum was measured after preparation in ambient air with ca. 30% humidity. **(bottom)** The Raman spectrum of the pristine single MOF crystal was recorded at 532 nm excitation with an integration time of 30 seconds under constant N_2 flow.

As expected from the molecular building blocks, the spectra of JUK-8 are strongly dominated by the signature of the linkers and contributions of solvent residues in particular DMF and water (Figure S6.4b). Besides the water signature centered at 3300 cm^{-1}, we see the trans/cis NH-stretching vibrations of the pip linker at 3539 and 3470 cm^{-1} and at 3395 and 3240 cm^{-1} due to EtOH and water molecules adsorbed to the pip linker ($pip{\cdot}EtOH{\cdot}H_2O$) in the IR spectrum,[54] we observe contributions of aromatic CH stretching vibrations of the linkers at 3068 cm^{-1} and aliphatic CH stretching vibrations around 2915 and 2850 cm^{-1} of the residual guest molecules. The NH-stretching vibration ν(NH) of pip is visible at 3240 cm^{-1}, while the CN-stretching vibration ν(C=N) shows up around 1620 cm^{-1}. The fingerprint region

is dominated by various modes of DMF (1657, 1094, and 876 cm^{-1}) and carboxylate-associated modes (1676, 1415, and 1159 cm^{-1}). Moreover, strong contributions of pyridine units at 1594, 1497, 1430, 1028, and 1008 cm^{-1} and stretching vibrations of various groups, including amide-, alkene-, and ester-moieties are observed between 1430 and 1050 cm^{-1}. Vibrational modes around 1000 cm^{-1} are associated with ring breathing, bending, and deformation modes of the pyridine units in pip. A summary of all vibrational modes in the IR spectrum and the corresponding pendant of Raman modes is given in Table S6.3.

Table S6.3. Band assignment for JUK-8. Abbreviations: ν: bond stretching; ρ: rocking (in-plane); δ: planar angle bending; β: in-plane bending; γ: out-of-plane bending (wagging); φ: deformation; τ: twisting; χ: aromatic ring breathing; i.p: in-plane; o.o.p: out-of-phase; sh: shoulder. BA: benzoic acid.

IR	Lit	Ref.	Assignment	Raman	Lit.	Ref.	Assignment
507							
535							
664	662	[47]	DMF: δ(O=C-N)	**663**	667	[47]	DMF: δ(O=C-N)
711	704	[51]	Pyridine: ρ(CH)				
783							
807	802	[43]	$\delta_s(COO^-)$				
824	814	[43]	$\delta_s(COO^-)$				
876	865	[47]	DMF: ν(N-CH_3)	**868**	866	[47]	DMF: ν(N-CH_3)
1008	1003	[51]	Pyridine: δ(CH) ring deformation	**997**	992	[52]	Pyridine: δ(CH) ring bending
1028	1030	[51]	Pyridine: δ(CH) ring bending	**1025**	1031	[52]	Pyridine: ν(CC+CN) ring breathing
1094	1091	[47]	DMF: γ(CH_3) N	**1079**	1093	[47]	DMF: γ(CH_3) N
1160	1160	[43]	δ(CH)	**1154**	1162	[47]	δ(CH)
				1213	1217	[52]	Pyridine: ν(C-N)
1261	1258	[43]	ν(C=C) / ν (C-N) / β(C-H)	**1243**	1243	[43]	ν(C=C) / ν (C-N) / β(C-H)
1296	1296	[43]	ν(C=C) / ν(N-H) / β(C-H)	**1298**	1296	[43]	ν(C=C) / ν(N-H) / β(C-H)
1383	1383	[43]	δ_s(CH)	**1325**	1321	[43]	ν(C-N)
1430	1437	[51]	Pyridine: β(CCH)				
1415	1415	[49]	ν_S(COO-)	**1425**	1425	[43]	ν(C–C) ring
1497	1481	[51]	Pyridine: β(CCH)	**1501**			ν(CN)
1559	1563	[49]	ν_{AS}(COO-)	**1552**			ν_{AS}(COO-)
1594	1995	[51]	Pyridine: ν(C=C) + β(CCH)	**1598**	1592	[52]	pyridine: ν(C=C)
1621	1619	[49]	Pip: ν(C=N)	**1625**			Pip: ν(C=N)
1657	1653	[47]	DMF: ν(C=O)	**1657**			DMF: ν(C=O)
1676	1687	[49]	Pip: ν(C=O)	**1675**			Pip: ν(C=O)
2850	---	[47]	DMF: aliphatic ν(CH)	**2844**			EtOH: aliphatic ν(CH)
2918	---	[47]	DMF: aliphatic ν(CH)	**2908**			EtOH: aliphatic ν(CH)
3068	--	[49]	Pip: aromatic ν(CH)	**3084**			Pip: aromatic ν(CH)
3240	--	[49]	Pip (H2O/EtOH): ν(NH) – cis				
3394	--	[49]	Pip (H2O/EtOH): ν(NH) – trans				
3470	--	[49]	Pip: ν(NH) – cis				
3539	--	[49]	Pip: ν(NH) – trans				

6.2.4. Carbonate solutions

At low pH, CO_2 converts via a first-order kinetic into carbonic acid H_2CO_3 with a half-life time of 26 ms at 25 °C showing a C-OH bending vibration in the Raman spectrum[53] at 1017 cm^{-1} (Figure S6.5). Carbonic acid H_2CO_3 further dissociates to bicarbonate HCO_3^-. This species can be monitored via three Raman resonances: (1) the symmetric C=O stretching band at 1365 cm^{-1}, (2) the bending mode at 1302 cm^{-1}, and (3) the C-OH bend mode at 1011 cm^{-1}, which is slightly shifted to lower wavenumbers. At basic pH, bicarbonate is further deprotonated and carbonate is formed at 1065 cm^{-1}.[55]

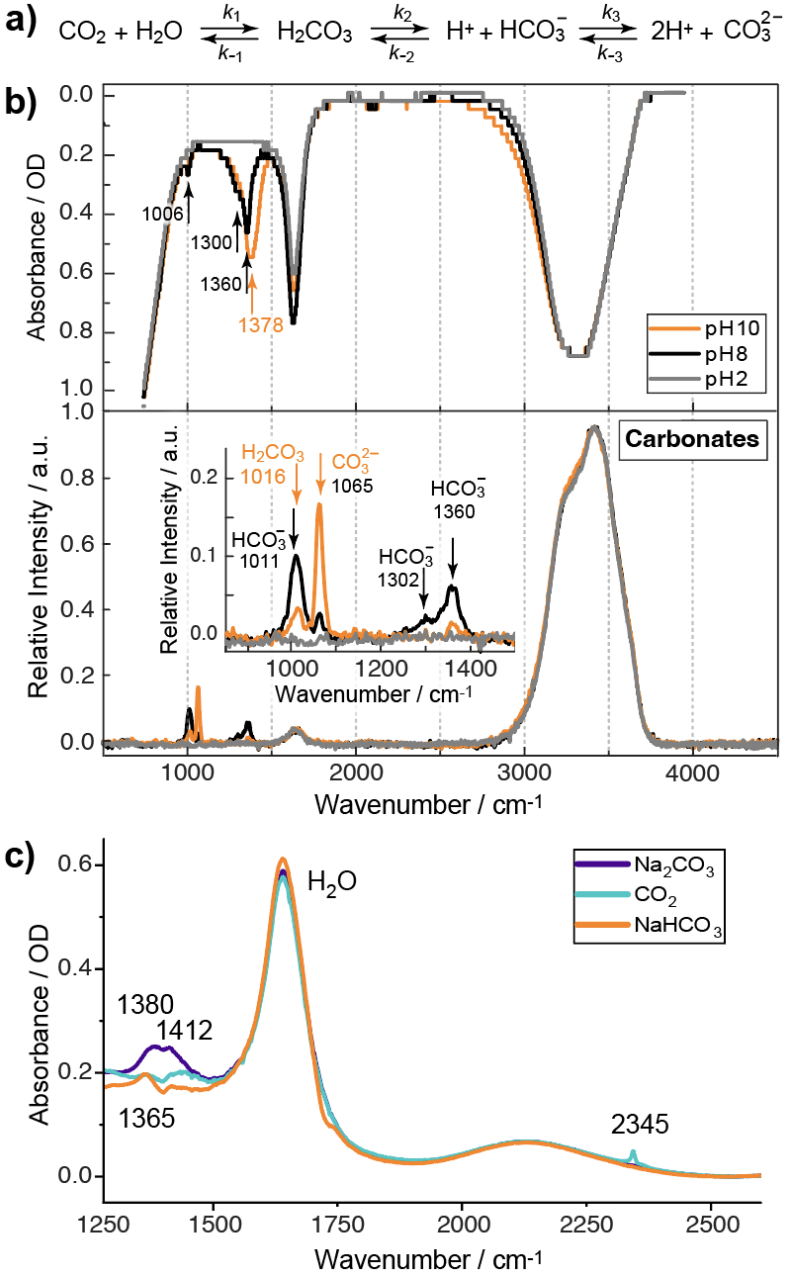

Figure S6.5. FTIR and Raman spectra of saturated $NaHCO_3$ solution as a function of pH. (a) Chemical equation of interconversion between CO_2, CO_3^{2-} and HCO_3^- where k_1, k_{-1}, k_2, k_{-2}, k_3, k_{-3} are the rate constants of each step. **(b)** The Raman spectra of the saturated solutions were recorded at 532 nm excitation with an integration time of 30 seconds in an open 8-well chamber microscope slide. **(c)** ATR-FTIR spectra of 150 mM saturated $NaHCO_3$, Na_2CO_3, and CO_2 in solution in a sealed ATR-FTIR flow cell.

The IR spectrum shows similar vibrational modes at 1006, 1300, and 1360 cm^{-1} for the bicarbonate band. In basic pH, however, the carbonate band does not show up around 1065 cm^{-1}, only the signature of bicarbonate is visible around 1410 cm^{-1}.[55] Nevertheless, both species, bicarbonate as well as carbonate, can be monitored via vibrational spectroscopic techniques. Dissolved CO_2 can be monitored at 2345 cm^{-1} via ATR-FTIR (Figure 6c) in a sealed flow chamber.

6.3. Characterization of host frameworks in water at pH 2, 6.3, 8.3, and 10

Next, we counterchecked whether differences in the pH values of the aqueous solution affect the vibrational signature of the hydroxylated MOF systems. Figure S6.6 shows the Raman spectra of UiO-66 and JUK-8 at different pH values.

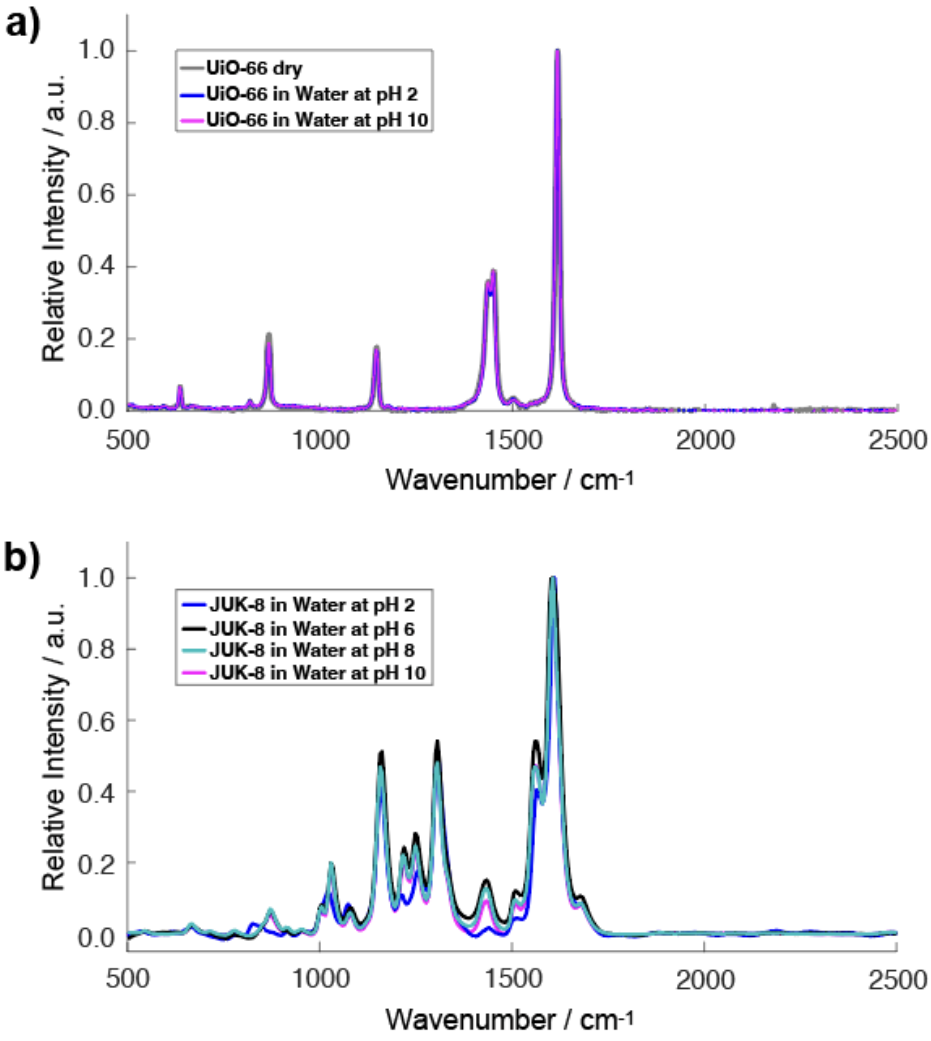

Figure S6.6. Raman spectra of MOF particles in water with different pH values. **(a)** Raman spectra of UiO-66 in dry form and in aqueous solution at pH 2 and pH 10 are identical. **(b)** Raman spectra of JUK-8 in aqueous solution at pH 2, 6.3, 8.3 and 10 reveal that JUK-8 is instable at low pH. Spectra were recorded with an excitation at 532 nm and an integration time of 30 seconds inside a 8-well chamber microscope slide.

In line with previous measurements presented in Supplementary Note S6.2, we do not observe any shift in the recorded spectra for UiO-66. While spectra of JUK-8 show minor changes in amplitude (after

normalization to 1660 cm^{-1}, most likely due to differences in the ratio between DMF guest molecules (1657 cm^{-1} and the pip linker (1621/1676 cm^{-1})), we do not observe a change in band position or the appearance of additional Raman transition for neutral and basic conditions. At a strongly acidic pH of pH 2, JUK-8 disassembles as revealed by shifts in Raman modes towards those of the free linker.

6.4. Raman mapping of water in JUK-8

We performed Hyper-spectral Raman experiments to monitor whether water can actually penetrate the MOF crystals or if we measure water layered between particles. To distinguish between water molecules that might have bound to the framework (during synthesis or storage) and water molecules that penetrate the framework afterwards, we employed deuterium oxide. We mapped free JUK-8 particles (featuring slow water uptake) in liquid D_2O and monitored the ν(OD) stretching vibration as function of space by space-resolved Raman spectroscopy. First, a XZ map was measured to find the middle plane of the crystal, at which the XY map was recorded afterwards. The XZ scan was measured at 1 mW/μm^2 to lower the risk of photodamaging the crystal. The XY scan was carried out at 18 mW μm^{-2} for better SNR. Both maps consist of 34×34 pixels and have a step-size of 1 or 2 µm within the XZ or XY area, respectively. The integration time per pixel amounted to 3s. The recorded hyperspectral data cubes were visualized by k-mean clustering.

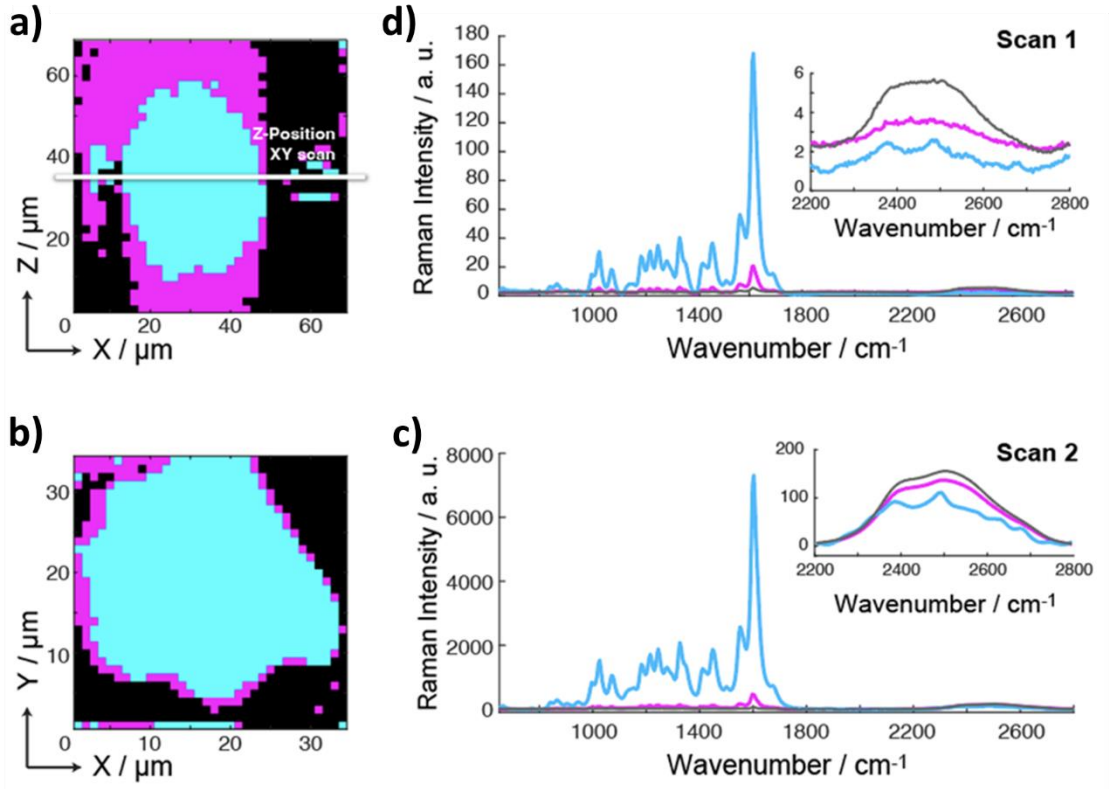

Figure S6.7. Uptake of deuterated water in JUK-8 monitored by Hyperspectral Raman imaging. a) XZ scan through a 68 x 68 μm^2 slice through JUK-8, directly after addition of D_2O. The white line in the middle of the crystal indicates the Z position for the XY scan. **b)** 34 x 34 μm^2 XY scan at the Z position through the crystal indicated in panel (a). Both Raman maps in (a) and (b) are derived by *k-mean* clustering with 3 clusters showing the surrounding D_2O (black) and D_2O incorporated in JUK-8 (pink, blue). **c)** Univariate Raman image showing

the distribution of D_2O within the XY scan based on the intensity of the ν(OD) stretching peak (2200 to 2800 cm^{-1}). **d)** Averaged Raman spectra in the respective clusters of the X-Y scan shown in panel (b).

Figure S6.7a-b shows the results of the XZ and XY images based on 3 clusters (the corresponding cluster spectra are depicted on the right). k-mean clustering reveals the shape of the JUK-8 particle in the two planes, which is surrounded by D_2O. For both hyperspectral data sets, we found that the black cluster corresponds to pure D_2O around of the crystal. The cyan cluster corresponds to the interior of JUK-8, which shows a reduced amount of D_2O that penetrated the framework. The pink cluster originates from areas at the interface between the MOF crystal and the liquid. Besides the overall lower signal in Figure S6.7a due to the reduced laser power, less D_2O penetrated the framework during the first scan (XZ; 0-60 min). During the second scan (XY; 60-120 min) the uptake of deuterium oxide saturated and reached on average 60% of the surrounding liquid.

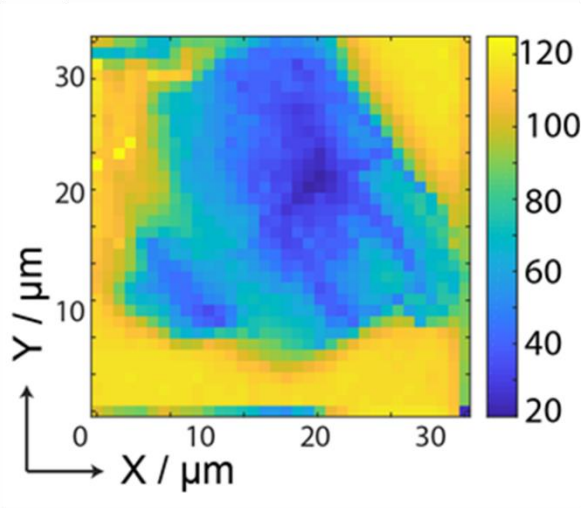

Figure S6.8. Univariate Raman imaging showing the distribution of deuterium oxide in JUK-8. The hyperspectral data set of the XY scan (34 x 34 $µm^2$) was evaluated by showing the Raman intensity of the ν(OD) stretching peak between 2200 and 2800 cm^{-1} as a function of space. High concentration of D_2O was found around the JUK-8 crystal matching the signal of the bare deuterium oxide.

Lastly, we investigated whether D_2O was taken up uniformly within the particle. For this, we visualized the spatial distribution of Raman intensity of the ν(OD) stretching peak between 2200 and 2800 cm^{-1} (Figure 6.8). D_2O penetrates the whole crystal. However, the distribution is not uniform and shows deviations between 15 and 75 % in concentration even after 1 hour of floating in D_2O.

6.5. Adsorption of carbonate species by metal-organic frameworks

Natural fresh and salt water sources usually show a slightly basic pH. To characterize which carbonate species might interact with UiO-66-NH_2 and JUK-8, we mimicked their possible adsorption at basic pH by exposing both MOF sample to 150 mM $NaHCO_3$ at pH 8.3. We chose ATR-FTIR for *time-resolved* measurements to identify the interacting species (Figure S6.9 and S6.10), and to monitor how fast and reversible their sorption behavior is (Figure S6.11 and S6.12).

6.5.1. IR spectra of UiO-66-NH_2 in $NaHCO_3$ solution at pH 8.3

Figure S6.9 shows the original data underlying Figure 4c in the manuscript (with background being a blank ATR crystal instead of the shown difference spectra in Figure 4c). As discussed in the main text, the presence of 150 mM aqueous solution of $NaHCO_3$ under basic conditions, leads to the formation of hydrogen carbonate ammonium salt between the amino-moiety of the linker and the carbonate, while replacing the $HCOO^-$ counter ion found in the pristine MOF. Their corresponding bands are found around 1600 and 1570 cm^{-1} ($\varphi(NH_3^+)$), which overlay with the $\nu_{as}(C{=}O)$.

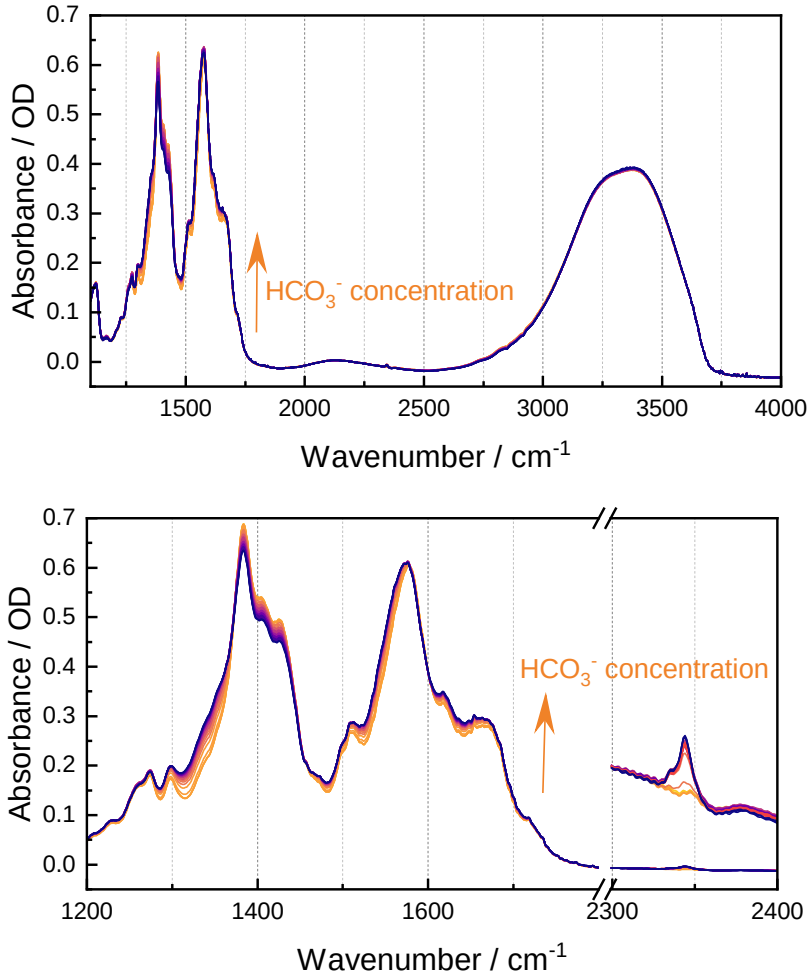

Figure S6.9. ATR-FTIR spectra of 150 mM $NaHCO_3$ solution adsorption into UiO-66-NH_2. Color scheme from organge to violet. (top) The ATR-FTIR spectrum was measured every 10s during the replacement of distilled water with the 150 mM $NaHCO_3$ solution with a flow speed of 1.5 ml min^{-1}. **(bottom)** Zoom into fingerprint region and dissolved CO_2 band at 2345 cm^{-1}. The shoulder of the latter band at 2336 cm^{-1} is associated with adsorbed CO_2 into the MOF scaffold.

6.5.2. IR spectra of JUK-8 in $NaHCO_3$ solution at pH 8.3

Figure S6.10 shows the original data underlying Figure 4d in the manuscript. As discussed in the main text, the presence of 150 mM aqueous solution of $NaHCO_3$ under basic conditions, leads to the formation of adsorbed polydentate (1400 – 1500 cm^{-1}), bicarbonate species (1660 cm^{-1}) and bidentate carbonate (1580 and 1274 cm^{-1}), as found for ZnO and ZrO_2 powders.[45–47]

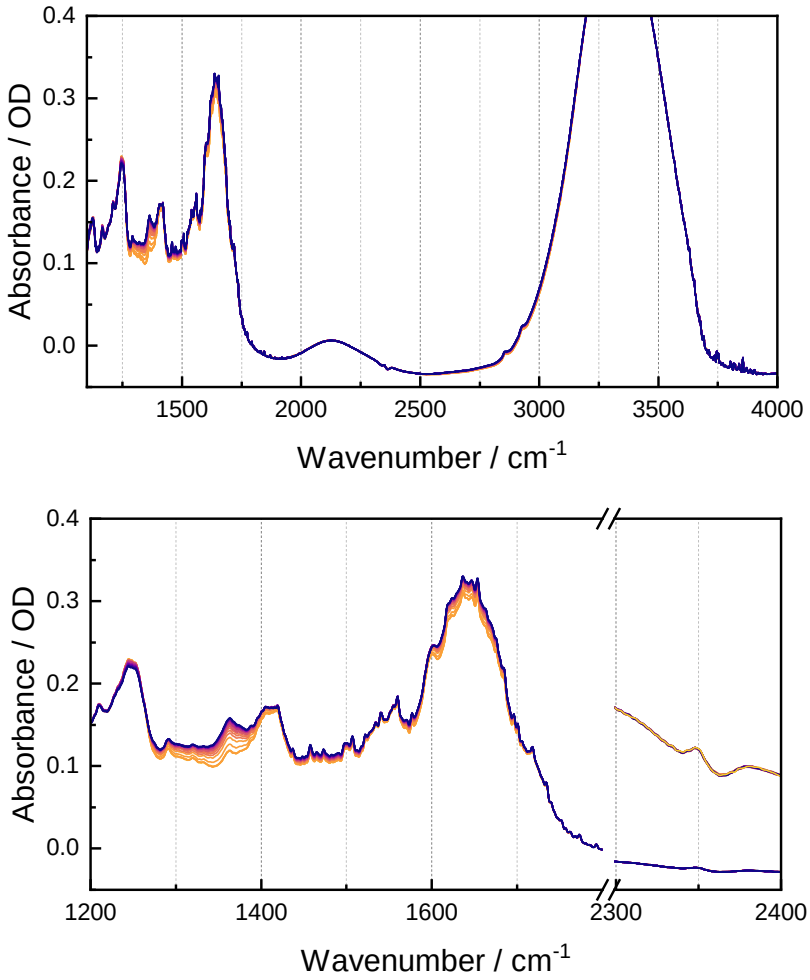

Figure S6.10. FTIR-ATR spectra of 150 mM $NaHCO_3$ solution adsorption into JUK-8. Color scheme from organge to violet. (top) The ATR-FTIR spectrum was measured every 10 s during the replacement of distilled water with the 150 mM $NaHCO_3$ solution with a flow speed of 1.5 ml min^{-1}. **(bottom)** Zoom into fingerprint region and dissolved CO_2 band at 2345 cm^{-1}.

6.5.3. Removal of unattached carbonate species by distilled water

Upon addition of 150 mmol/l $NaHCO_3$ solution, carbonate, and bicarbonate ions interact with the framework of UiO-66-NH_2 and JUK-8 (Figure 4). In order to evaluate the reversibility of the adsorption process, we exchanged the carbonate solution afterwards by distilled water, and flushed the flow cell with 300x volumes of water. For both sample systems, solvent exchange does not disturb the host framework. Bands associated with dissolved carbonate vanish, while bands associated with the adsorbed carbonate species remain indicating a permanent interaction with the host framework. In the case of UiO-66-NH_2, the disappearance of the carboxylic acid salt (bands around 1400 cm^{-1}) together with the incorporation of carbonate species, indicates the formation of ammonium carboxylates of the bicarbonate ions with the amine-group of the linker molecules (Figure S6.11). In the case of JUK-8, an irreversible uptake and interaction with the MOF framework of carbonate and bicarbonate species is observed (Figure S6.12).

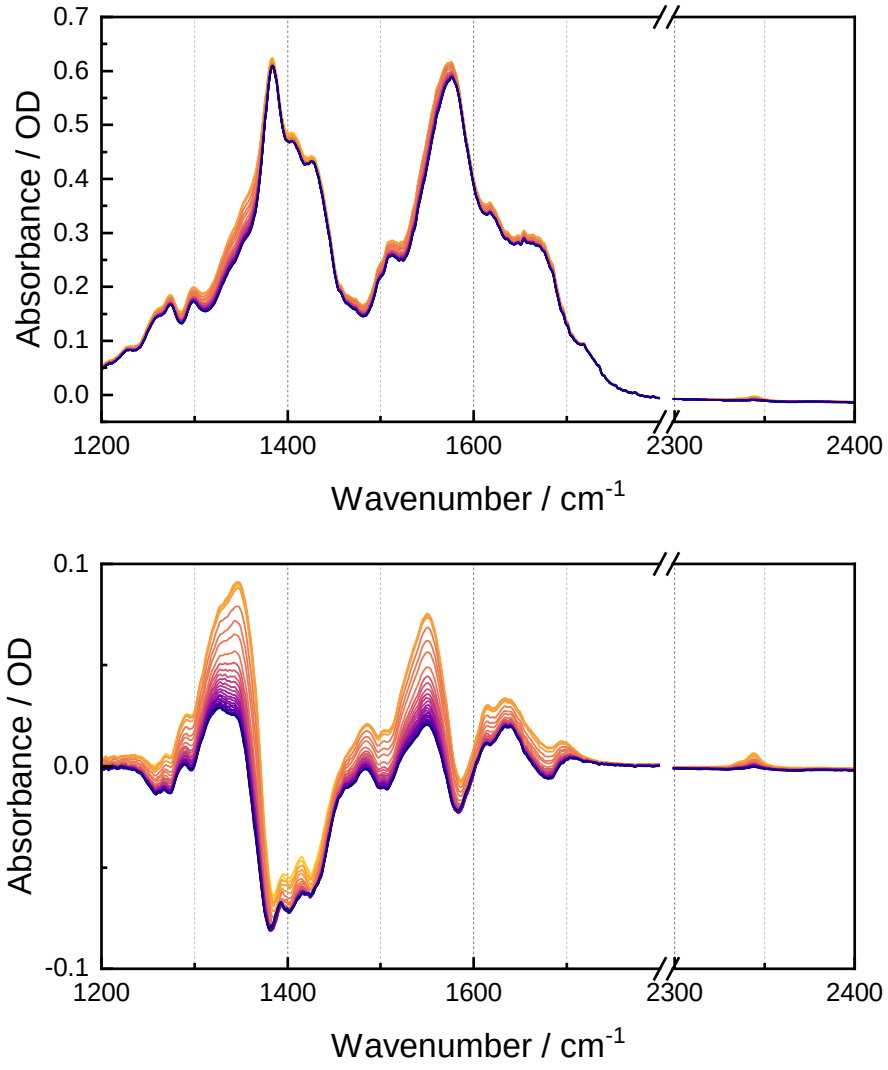

Figure S6.11. FTIR-ATR spectra during replacement of 150 mmol/l $NaHCO_3$ solution with distilled water in UiO-66-NH_2. Color scheme from organge to violet. (top) The ATR-FTIR spectrum was measured every 10 s during the replacement of 150 mmol/l $NaHCO_3$ solution with distilled water with a flow speed of 1.5 ml min^{-1}. **(bottom)** Difference spectra of (top) spectra obtained from a background spectra recorded prior to carbonate application.

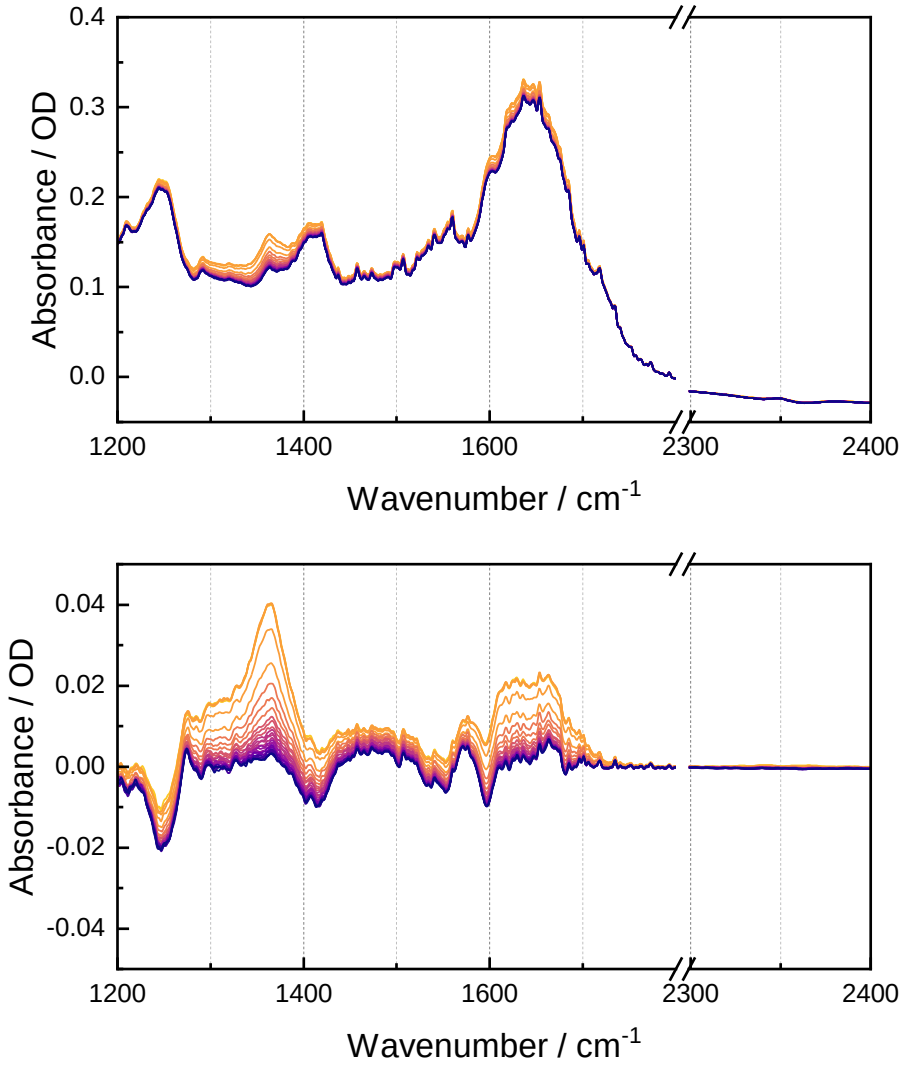

Figure S6.12. ATR-FTIR spectra during replacement of 150 mmol/l $NaHCO_3$ solution with distilled water in JUK-8. Color scheme from organge to violet. (top) The ATR-FTIR spectrum was measured every 10 s during the replacement of 150 mmol/l $NaHCO_3$ solution with distilled water with a flow speed of 1.5 ml min^{-1}. **(bottom)** Difference spectra of (top) spectra obtained from a background spectra recorded prior to carbonate application.

6.6. CO_2 adsorption to JUK-8 and UiO-66-NH_2 in gas phase

For comparison with traditionally reported gas-phase adsorption experiments, we replaced the liquid-handling system of the ATR-FTIR setup with a gas mixer (see further experimental details in Section 1.11 and scheme in Figure S6.13) composed of three mass flow controllers (MFCs). FTIR-ATR spectra were recorded during the application of CO_2 and water vapor. Adsorption of CO_2 into pristine MOFs yielded a sharp band at 2340 cm^{-1}, which is redshifted from the gas phase band position because of interactions of CO_2 with the MOF.[56] In addition, for UiO-66-NH_2, a negative band at 3670 cm^{-1} indicates the interaction of CO_2 with the free OH-groups of the Zr-cluster. This band is not visible for JUK-8 that lacks OH-groups. Furthermore, only neglectable changes of the spectra in the fingerprint region of both MOFs were observed, which indicate only minor interactions with the framework during CO_2 adsorption. Note that no spectral changes were observed after replacing CO_2 with N_2, confirming no structural changes of the MOF induced by CO_2 adsorption from gas phase or remaining, captured CO_2. The CO_2 adsorption experiment was repeated after wetting the MOF films with 80 % humidity and showed no changes in sorption capacity or band position.

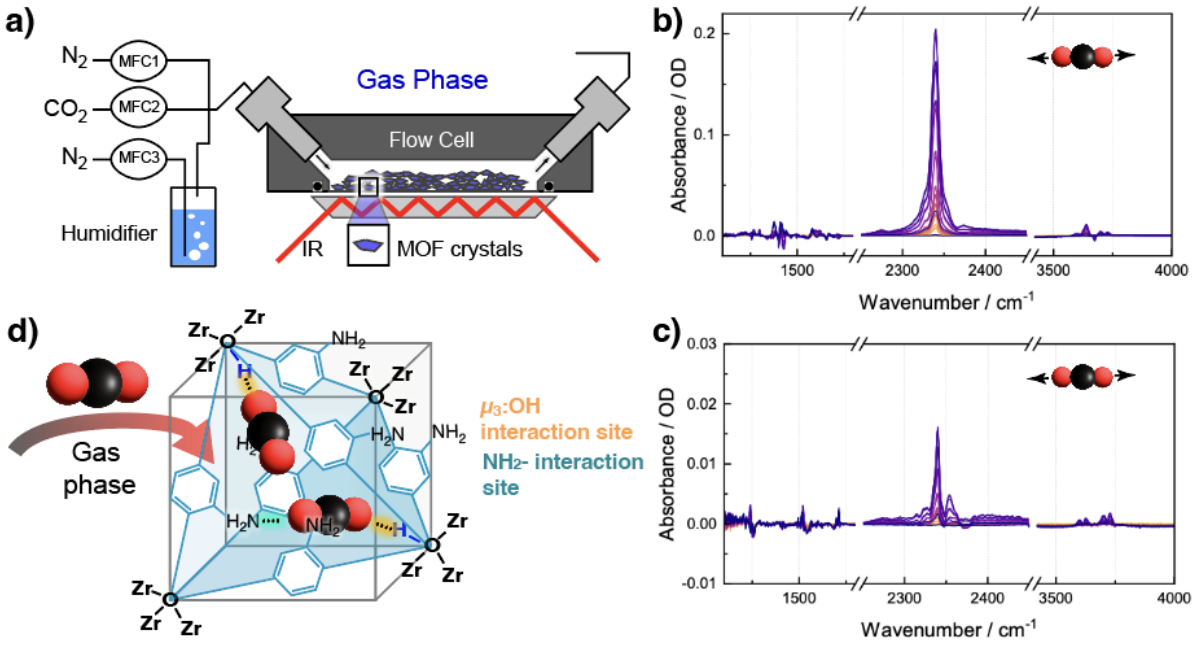

Figure S6.13. Spectroscopic evaluation of CO_2 adsorption by UiO-66-NH_2 and JUK-8 in gas phase. **a)** Schematic ATR-FTIR setup for transient spectroscopy to follow CO_2 adsorption to MOFs in gas phase. **b-c)** Difference ATR-FTIR spectra after addition of 0 – 0.8 p(CO_2) to **b)** UiO-66-NH_2 and **c)** JUK-8 show an increased amount of CO_2 and adsorption of guest molecule to the frameworks. The reference/background spectrum was recorded for MOFs exposed to N_2 in the flow cell and gas phase CO_2 bands were subtracted**. d)** Interaction mechanism of CO_2 with UiO-66-NH_2 in gas phase.

6.7. CO_2 adsorption to JUK-8 and UiO-66-NH_2 in the gas phase in presence of water

Next, we characterized the amount of adsorbed CO_2 in the presence of water. For this, we monitored the height of the IR absorbance centered at 3470 cm^{-1} (in the case of water) and 2340 cm^{-1} (in the case of carbon dioxide) as a function of applied relative humidity. As shown in Figure S6.14, water molecules adsorb to the framework of both MOF systems. The water uptake in UiO-66-NH_2 follows a Type IV hysteresis with a steep rise of adsorbed water upon pore condensation at p/p_0 = 0.3.[57-58] JUK-8 shows a more complex behavior with an increase of adsorbed water low water vapor pressure (p/p_0=0.1) followed by a gradual increase until p/p_0=0.6 and a second steep increase at p/p_0=9. This observation is in line with the gate restructuring processes that have been observed for JUK-8.[59] As seen in Figure S6.14, carbon dioxide adsorbs to both MOF systems in the gas phase monitored by absorbance at 2340 cm^{-1} of 0.1 OD in UiO-66-NH_2 and 0.02 OD in JUK-8 at a partial pressure of 0.2. In the presence of water vapor, this uptake is reduced by 50 % already in presence of ~20 %RH in the case of UiO-66-NH_2, and even more in JUK-8, which shows a 50 % reduction already below 10 %RH (Supplementary Note 6.3). The height of the CO_2 band stabilizes after pore condensation at 0.01 OD for UiO-66-NH_2, while no adsorbed CO_2 was detected for JUK for RH>0.2. Both experiments show, that carbon dioxide preferably binds to an empty framework. These findings obtained from gas-phase adsorption experiments are in line with aqueous phase adsorption, where a band of adsorbed CO_2 was observed for UiO-66-NH_2 but not for JUK-8.

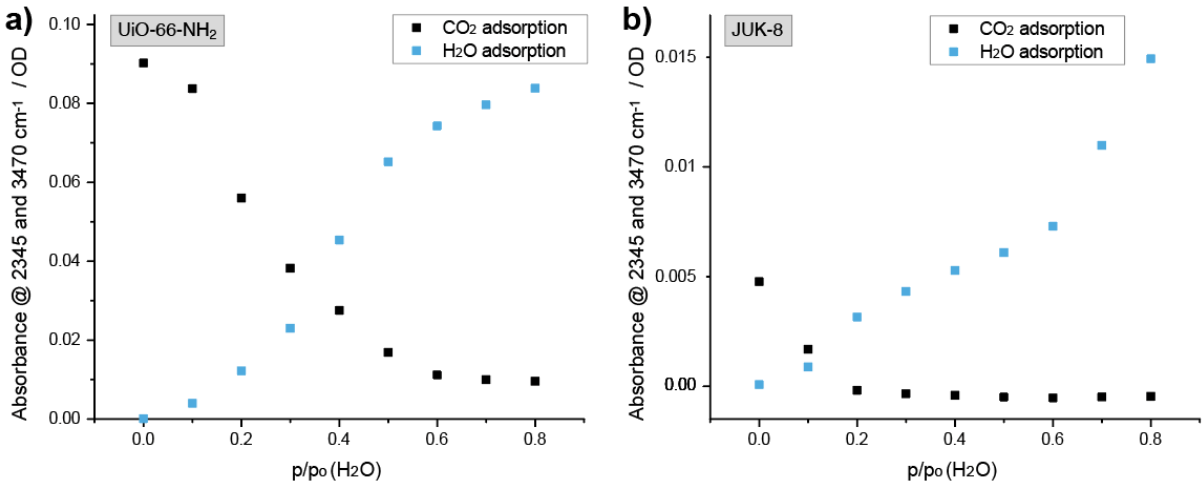

Figure S6.14. Uptake of water, respectively CO_2, in presence of water in (a) UiO-66-NH2 and (b) JUK-8. The intensity at 3470 cm^{-1} (water) and 2340 cm^{-1} (CO_2) was depicted as a function of relative humidity and served for monitoring the amount of adsorbed guest molecules.

SUPPLEMENTARY NOTE 7. REAL-WORLD WATER SAMPLES

Real-world water samples were collected at five different locations along the East coast of Spain (Figure S7.1; Table S7.1), in particular, along the coast of the Mediterranean Sea, i.e., around Mataró and in the Pletera lagoon, the Tordera river and the water reservoirs of the Foix and Colomers rivers. The locations were chosen such that samples from salt and fresh water were taken into account, as well as conditions of free (ocean), flowing (river), and retained (reservoirs) water in a similar climatic region could be incorporated into the study.

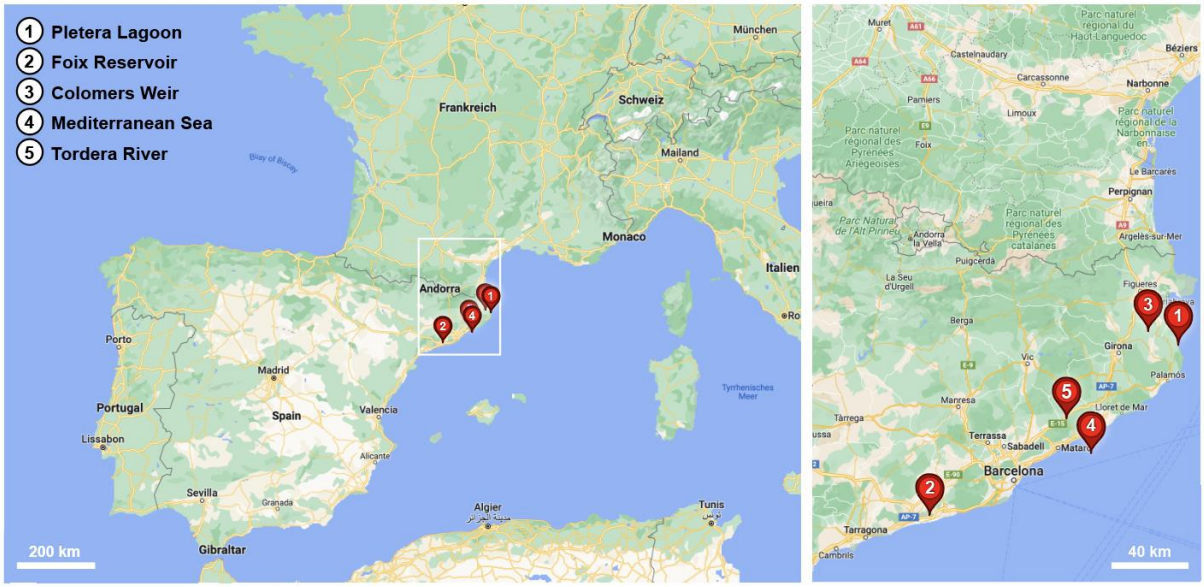

Figure S7.1. Selected sampling sites along the East coast of Spain. Water samples were collected in the Mediterranean Sea, at the coast at Mataró (4) and the Pletera lagoon (1), in the Tordera river (5), and in the reservoirs of the Foix (2) and Colomers rivers (3). The locations are numbered and marked in red.

All samples were characterized via in-field measurements, together with their location and environmental conditions such as the temperature, atmospheric pressure, and the partial pressure of CO_2. The parameters are summarized in Tables S7.1 and S7.2.

Table S7.1. Collection sites and environmental parameters. Samples were collected and characterized in-field. NA: not applicable.

#	Sample	Latitude	Longitude	Temperature	Atmospheric pressure	CO_2 partial pressure
				(°C)	(mm Hg)	(µ-atm)
1	Pletera Lagoon	42.0312135	3.1906245	15,3	769,5	289
2	Foix Reservoir	41.2544287	1.6440742	11,6	760,6	2352
3	Colomers Weir	42.0769462	2.9915725	13,1	767,3	2541
4	Mediterranean Sea	41.5780474	2.5506917	NA	NA	NA
5	Tordera River	41.6858087	2.4972243	11,2	758,7	884

7.1. Composition of collected water samples

To link our findings to the chemical composition of ions and elements dissolved in the collected water samples, we characterized various physicochemical parameters. Samples were collected at different locations and filtered through a 200-µm cut-off membrane. The brine salinity (expressed electrical conductivity), pH, and dissolved oxygen concentration were measured in-field. In addition, alkalinity titrations and HTC measurements were carried out in the lab to derive the alkalinity and the total inorganic carbon (TIC) concentration of the collected samples (Table S7.2). As expected, saltwater samples (collected in the Pletera Lagoon and the Mediterranean Sea) contain more ions and hence show a higher electrical conductivity compared to freshwater samples. While the pH is fairly constant around pH 8, the alkalinity varies at maximum by a factor of 5, similar to the total amount of measured bicarbonate HCO_3^-, which is the most abundant species in a moderate basic environment.

Table S7.2. Physicochemical parameter of collected water samples. Since the addition of the CO_2 to water lowers the pH, while the alkalinity is not affected, we further quantified the electrical conductivity and the amount of dissolved CO_2 species.

#	Sample	Alkalinity	pH	Electrical conductivity	TIC
		(meq/l)		@25 ºC (µS / cm)	(mmol/l of HCO_3^-)
1	Pletera Lagoon	7.086	8.38	43000.0	4.73078172
2	Foix Reservoir	4.636	8.26	1187.0	3.899855962
3	Colomers Weir	3.072	8.28	533.0	2.499438001
4	Mediterranean Sea	2.756	8.03	52100.0	2.106455078
5	Tordera River	1.201	7.99	219.0	0.949986262

7.2. Carbonate adsorption from different bodies of water

Lastly, we investigated the uptake capacities of MOFs for carbon species from real-world water samples. For this, we exposed MOF-74(Ni), UiO-66, UiO-66-NH_2, ZU-301, Cu-TDPAT, MIL-127, and JUK-8 to different water samples, by adding 25 ml of water to 25 mg of MOF powder. The mixtures were shaken for 4 h after water addition, followed by materials separation as described in Supplementary Note S5. Next, the initial and final total inorganic carbon (TIC) concentrations were measured by high-temperature combustion. The removal efficiency R was determined as the ratio between the final and initial TIC concentration (Table S7.3), i.e., the TIC values of the collected water and the water after exposure to the various MOF samples.

$$R = \frac{\mathrm{TIC}_{final}}{\mathrm{TIC}_{initial}} \times 100 \qquad \text{(eq. 7.1)}$$

We see a strong dependency on the water composition, nevertheless, all tested MOF systems lead to a reduction of the dissolved carbon content. While JUK-8, ZU-301, and MOF-74(Ni) show an average removal efficiency below 5%, all other MOF systems reduce the carbon concentration on average by around 30%, with up to 48 and 59% even in the case of UiO66-NH_2 and MIL-127, respectively. Empirically, we observed that the removal efficiency strongly depends on the ion composition of the water, as represented by the alkalinity of the water: the lower these parameters are, the higher the removal efficiency is. The electrical conductivity, and as such the brine salinity, follows the same trend, except for water from the Mediterranean Sea.

Table S7.3: Uptake of carbon species from real-world water samples.

Material	**Removal efficiency in %**				
	Pletera Lagoon	**Foix Reservoir**	**Colomers Weir**	**Mediterranean Sea**	**Tordera River**
MOF-74(Ni)	2.34	2.33	0.57	ND	ND
MIL-127	13.20	26.09	38.41	40.40	58.58
Cu-TDPAT	8.69	19.43	37.61	40.67	35.50
UiO-66	17.10	29.66	19.45	27.62	30.64
UiO-66-NH_2	22.84	29.65	29.81	39.33	48.19
ZU-301	2.34	1.86	3.53	3.79	0.96
JUK-8	ND	1.05	8.86	2.37	4.12

REFERENCES

1. Rouquerol, J., Llewellyn, P. & Rouquerol, F. Is the bet equation applicable to microporous adsorbents? *Stud. Surf. Sci. Catal.***, 160,** 49–56, (2007).
2. Fuchs, A. *et al.* Single Crystals Heterogeneity Impacts the Intrinsic and Extrinsic Properties of Metal-Organic Frameworks. *Adv. Mater.***, 34,** e2104530, (2022).
3. Schrimpf, W., Barth, A., Hendrix, J. & Lamb, D. C. PAM: A Framework for Integrated Analysis of Imaging, Single-Molecule, and Ensemble Fluorescence Data. *Biophysical journal***, 114,** 1518–1528, (2018).
4. Schneider, C. A., Rasband, W. S. & Eliceiri, K. W. NIH Image to ImageJ: 25 years of image analysis. *Nature methods***, 9,** 671–675, (2012).
5. Baumgartner, B., Prins, P. T., Louwen, J. N., Monai, M. & Weckhuysen, B. M., The Role of water in carbon dioxide adsorption in porphyrinic metal-organic frameworks, *ChemCatChem*, e202300722 (2023).
6. Baumgartner, B., Hayden, J., Schwaighofer, A. & Lendl, B., In Situ IR Spectroscopy of Mesoporous Silica Films for Monitoring Adsorption Processes and Trace Analysis, *ACS Appl. Nano Mater*. **1, 12**, 7083–7091, (2018).
7. Pettersen, E. F. *et al.* UCSF Chimera--a visualization system for exploratory research and analysis. *J. Comput. Chem.***, 25,** 1605–1612, (2004).
8. Knoche, W. (1980). Chemical Reactions of CO_2 in Water. In: Bauer, C., Gros, G., Bartels, H. (eds) Biophysics and Physiology of Carbon Dioxide. Proceedings in Life Sciences. Springer, Berlin, Heidelberg. https://doi.org/10.1007/978-3-642-67572-0_1.
9. Hurd, C. L., Lenton, A., Tilbrook, B., Boyd, P. W., Nature Clim Change 8, 686–694 (2018).
10. Kim, S., Nitzsche, M. P., Rufer, S. B., Lake, J. R., Varanasi, K. K., Hatton, T. A., Energy Environ. Sci., 16, 2030–2044, (2023).
11. Caskey, S. R., Wong-Foy, A. G. & Matzger, A. J. Dramatic tuning of carbon dioxide uptake via metal substitution in a coordination polymer with cylindrical pores. *J. Am. Chem. Soc.***, 130,** 10870–10871, (2008).
12. An, J., Geib, S. J. & Rosi, N. L. High and selective CO2 uptake in a cobalt adeninate metal-organic framework exhibiting pyrimidine- and amino-decorated pores. *J. Am. Chem. Soc.***, 132,** 38–39, (2010).
13. Li, B. *et al.* Enhanced Binding Affinity, Remarkable Selectivity, and High Capacity of CO2 by Dual Functionalization of a rht-Type Metal-Organic Framework. *Angew. Chem. Int. Ed.***, 124,** 1441–1444, (2012).
14. Nugent, P. *et al.* Porous materials with optimal adsorption thermodynamics and kinetics for CO2 separation. *Nature***, 495,** 80–84, (2013).
15. Saha, D., Bao, Z., Jia, F., Deng, S., Adsorption of CO_2, CH_4, N_2O, and N_2 on MOF-5, MOF-177, and Zeolite 5A, *Environ. Sci. Technol.*, **44**, **5**, 1820–1826 (2010).

16. Wongsakulphasatch, S. *et al.* Effect of Fe open metal site in metal-organic frameworks on post-combustion CO 2 capture performance. *Greenhouse Gas Sci. Technol.***, 7,** 383–394, (2017).
17. Jiang, M. *et al.* Controlling Pore Shape and Size of Interpenetrated Anion-Pillared Ultramicroporous Materials Enables Molecular Sieving of CO2 Combined with Ultrahigh Uptake Capacity. *ACS Appl. Mater. Interfaces***, 10,** 16628–16635, (2018).
18. Huang, A., Wan, L. & Caro, J. Microwave-assisted synthesis of well-shaped UiO-66-NH2 with high CO2 adsorption capacity. *Mater. Res. Bull.***, 98,** 308–313, (2018).
19. Koutsianos, A., Kazimierska, E., Barron, A. R., Taddei, M. & Andreoli, E. A new approach to enhancing the CO2 capture performance of defective UiO-66 via post-synthetic defect exchange. *Dalton Trans.***, 48,** 3349–3359, (2019).
20. Liu, Y., Ghimire, P. & Jaroniec, M. Copper benzene-1,3,5-tricarboxylate (Cu-BTC) metal-organic framework (MOF) and porous carbon composites as efficient carbon dioxide adsorbents. *J. Colloid Interface Sci.***, 535,** 122–132, (2019).
21. Li, Q., Guo, J., Zhu, H. & Yan, F. Space-Confined Synthesis of ZIF-67 Nanoparticles in Hollow Carbon Nanospheres for CO2 Adsorption. *Small***, 15,** e1804874, (2019).
22. Park, J. M., Yoo, D. K. & Jhung, S. H. Selective CO2 adsorption over functionalized Zr-based metal organic framework under atmospheric or lower pressure: Contribution of functional groups to adsorption. *Chem. Eng. J.***, 402,** 126254, (2020).
23. Liao, J. *et al.* Highly efficient CO 2 capture and conversion of a microporous acylamide functionalized rht -type metal–organic framework. *Inorg. Chem. Front.***, 7,** 1939–1948, (2020).
24. He, T., Xiao, Y., Zhao, Q., Zhou, M. & He, G. Ultramicroporous Metal–Organic Framework Qc-5-Cu for Highly Selective Adsorption of CO 2 from C 2 H 4 Stream. *Ind. Eng. Chem. Res.***, 59,** 3153–3161, (2020).
25. Zhang, Z. *et al.* Mechano-assisted synthesis of an ultramicroporous metal-organic framework for trace CO2 capture. *Chem. Commun.***, 56,** 7726–7729, (2020).
26. Yu, C. *et al.* Selective capture of carbon dioxide from humid gases over a wide temperature range using a robust metal–organic framework. *Chem. Eng. J.***, 405,** 126937, (2021).
27. Roztocki, K. *et al.* Combining In Situ Techniques (XRD, IR, and 13C NMR) and Gas Adsorption Measurements Reveals CO2-Induced Structural Transitions and High CO2/CH4 Selectivity for a Flexible Metal-Organic Framework JUK-8. *ACS Appl. Mater. Interfaces***, 13,** 28503–28513, (2021).
28. Øien, S. *et al.* Detailed Structure Analysis of Atomic Positions and Defects in Zirconium Metal–Organic Frameworks. *Cryst. Growth Des.***, 14,** 5370–5372, (2014).
29. Wong-Ng, W., Kaduk, J. A., Wu, H. & Suchomel, M. Synchrotron X-ray studies of metal-organic framework M2 (2,5-dihydroxyterephthalate), M = (Mn, Co, Ni, Zn) (MOF74). *Powder Diffr.***, 27,** 256–262, (2012).

30. Drake, H. F. *et al.* The thermally induced decarboxylation mechanism of a mixed-oxidation state carboxylate-based iron metal-organic framework. *Chem. Commun.***, 55,** 12769–12772, (2019).
31. Luebke, R. *et al.* The unique rht-MOF platform, ideal for pinpointing the functionalization and CO2 adsorption relationship. *Chem. Commun.***, 48,** 1455–1457, (2012).
32. Trickett, C. A. *et al.* Definitive molecular level characterization of defects in UiO-66 crystals. *Angewandte Chemie (International ed. in English)***, 54,** 11162–11167, (2015).
33. Chevreau, H. *et al.* Synthesis of the biocompatible and highly stable MIL-127(Fe): from large scale synthesis to particle size control. *CrystEngComm***, 18,** 4094–4101, (2016).
34. Li, B. *et al.* Enhanced binding affinity, remarkable selectivity, and high capacity of CO2 by dual functionalization of a rht-type metal-organic framework. *Angew. Chem. Int. Ed.***, 51,** 1412–1415, (2012).
35. Roztocki, K. *et al.* Collective Breathing in an Eightfold Interpenetrated Metal-Organic Framework: From Mechanistic Understanding towards Threshold Sensing Architectures. *Angew. Chem. Int. Ed.***, 59,** 4491–4497, (2020).
36. Stone, K. A., He, Q. P. & Wang, J. Two Experimental Protocols for Accurate Measurement of Gas Component Uptake and Production Rates in Bioconversion Processes. *Scientific reports***, 9,** 5899, (2019).
37. König, M., Vaes, J., Klemm, E. & Pant, D. Solvents and Supporting Electrolytes in the Electrocatalytic Reduction of CO2. *iScience***, 19,** 135–160, (2019).
38. Allesson, L. *et al.* Drivers and variability of CO2:O2 saturation along a gradient from boreal to Arctic lakes. *Scientific reports***, 12,** 18989, (2022).
39. Halewood, E. *et al.* Determination of dissolved organic carbon and total dissolved nitrogen in seawater using High Temperature Combustion Analysis. *Front. Mar. Sci.***, 9,** 95, (2022).
40. Shearer, G. C. *et al.* Tuned to Perfection: Ironing Out the Defects in Metal–Organic Framework UiO-66. *Chemistry of Materials* **26**, 4068-4071, doi:10.1021/cm501859p (2014).
41. Fairley, M. *et al.* Linker Contribution toward Stability of Metal–Organic Frameworks under Ionizing Radiation. *Chemistry of Materials* **33**, 9285-9294, doi:10.1021/acs.chemmater.1c02999 (2021).
42. Grissom, T. G. *et al.* Benzene, Toluene, and Xylene Transport through UiO-66: Diffusion Rates, Energetics, and the Role of Hydrogen Bonding. *The Journal of Physical Chemistry C* **122**, 16060-16069, doi:10.1021/acs.jpcc.8b03356 (2018).
43. Hadjiivanov, K. I. *et al.* Power of Infrared and Raman Spectroscopies to Characterize Metal-Organic Frameworks and Investigate Their Interaction with Guest Molecules. *Chemical Reviews* **121**, 1286-1424, doi:10.1021/acs.chemrev.0c00487 (2021).
44. Kandiah, M. *et al.* Synthesis and Stability of Tagged UiO-66 Zr-MOFs. *Chemistry of Materials* **22**, 6632-6640, doi:10.1021/cm102601v (2010).

45. Cavka, J. H. *et al.* A New Zirconium Inorganic Building Brick Forming Metal Organic Frameworks with Exceptional Stability. *Journal of the American Chemical Society* **130**, 13850-13851, doi:10.1021/ja8057953 (2008).
46. Ethiraj, J. *et al.* Carbon Dioxide Adsorption in Amine-Functionalized Mixed-Ligand Metal–Organic Frameworks of UiO-66 Topology. *ChemSusChem* **7**, 3382-3388, doi:https://doi.org/10.1002/cssc.201402694 (2014).
47. Venkata Chalapathi, V. & Venkata Ramiah, K. Normal vibrations of N, N-dimethylformamide and N, N-dimethylacetamide. *Proceedings of the Indian Academy of Sciences - Section A* **68**, 109-122, doi:10.1007/BF03049367 (1968).
48. Kandiah, M. *et al.* Post-synthetic modification of the metal–organic framework compound UiO-66. *Journal of Materials Chemistry* **20**, 9848-9851, doi:10.1039/C0JM02416C (2010).
49. Roztocki, K. *et al.* Collective Breathing in an Eightfold Interpenetrated Metal–Organic Framework: From Mechanistic Understanding towards Threshold Sensing Architectures. *Angewandte Chemie International Edition* **59**, 4491-4497, doi:https://doi.org/10.1002/anie.201914198 (2020).
50. Formalik, F., Neimark, A. V., Rogacka, J., Firlej, L. & Kuchta, B. Pore opening and breathing transitions in metal-organic frameworks: Coupling adsorption and deformation. *Journal of Colloid and Interface Science* **578**, 77-88, doi:https://doi.org/10.1016/j.jcis.2020.05.105 (2020).
51. Perelygin, I. S. & Klimchuk, M. A. Infrared spectra of coordinated pyridine. *Journal of Applied Spectroscopy* **24**, 43-46, doi:10.1007/BF01100716 (1976).
52. Pagliai, M., Bellucci, L., Muniz-Miranda, M., Cardini, G. & Schettino, V. A combined Raman, DFT and MD study of the solvation dynamics and the adsorption process of pyridine in silver hydrosols. *Physical Chemistry Chemical Physics* **8**, 171-178, doi:10.1039/B509976E (2006).
53. Falcke, H. & Eberle, S. H. Raman spectroscopic identification of carbonic acid. *Water Research* **24**, 685-688, doi:https://doi.org/10.1016/0043-1354(90)90023-Y (1990).
54. Roztocki, K., Formalik, F., Krawczuk, A., Senkovska, I., Kuchta, B., Kaskel, S., Matoga, D., Collective breathing in an eightfold interpenetrated metal–organic framework: from mechanistic understanding towards threshold sensing architectures, *Angew. Chem. Int. Ed.*, **59**, 4491 – 4497, (2020).
55. Oliver, B. G., Davis, A. R., Vibrational spectroscopic studies of aqueous alkali metal bicarbonate and carbonate solutions. *Can. J.Chem.*, **51**, 698−702 (1973).
56. Hadjiivanov, K. I., Panayotov, D. A., Mihaylov, M. Y., Ivanova, E. Z., Chakarova, K. K., Andonova, S. M., Drenchev, N. L., Power of infrared and raman spectroscopies to characterize metal-organic frameworks and investigate their interaction with guest molecules, *Chem. Rev.*, **121, 3**, 1286–1424 (2021).

57. Baumgartner, B., Hayden, J., Loizillon, J., Steinbacher, S., Grosso, D., Lendl, B., Pore size-dependent structure of confined water in mesoporous silica films from water adsorption/desorption using ATR–FTIR spectroscopy, *Langmuir*, **35, 37**, 11986–11994, (2019).
58. Thommes, M., Kaneko, K., Neimark, A. V., Olivier, J. P., Rodriguez-Reinoso, F., Rouquerol, J., Sing, K. S.W., Physisorption of gases, with special reference to the evaluation of surface area and pore size distribution (IUPAC Technical Report), *Pure and Applied Chemistry*, **87**, **9-10**, 1051-1069, (2015).
59. Roztocki, K., Rauche, M., Bon, V., Kaskel, S., Brunner, E., Matoga, D., Combining in situ techniques (XRD, IR, and ^{13}C NMR) and gas adsorption measurements reveals CO_2-induced structural transitions and high CO_2/CH_4 selectivity for a flexible metal–organic framework JUK-8, *ACS Appl. Mater. Interfaces*, **13, 24**, 28503–28513 (2021).
60. Gazioğlu, C., Müftüoğlu, E., Demir, V., Aksu, A., Okutan, V., Connection between ocean acidification and sound propagation, *International Journal of Environment and Geoinformatics* **2 (2)**, 16–26 (2015).